

NASA TECHNICAL NOTE



NASA TN D-3343

NASA TN D-3343

LOAN COPY: RETURN TO
AFWL (WHL-2)
KIRTLAND AFB, N MEX

0130624



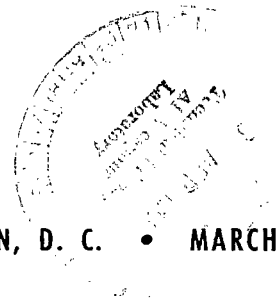
TECH LIBRARY KAFB, NM

SUMMARY OF FULL-SCALE LIFT AND DRAG CHARACTERISTICS OF THE X-15 AIRPLANE

by Edwin J. Saltzman and Darwin J. Garringer

*Flight Research Center
Edwards, Calif.*

NATIONAL AERONAUTICS AND SPACE ADMINISTRATION • WASHINGTON, D. C. • MARCH 1966





SUMMARY OF FULL-SCALE LIFT AND DRAG CHARACTERISTICS
OF THE X-15 AIRPLANE

By Edwin J. Saltzman and Darwin J. Garringer

Flight Research Center
Edwards, Calif.

NATIONAL AERONAUTICS AND SPACE ADMINISTRATION

For sale by the Clearinghouse for Federal Scientific and Technical Information
Springfield, Virginia 22151 – Price \$0.70

SUMMARY OF FULL-SCALE LIFT AND DRAG CHARACTERISTICS
OF THE X-15 AIRPLANE

By Edwin J. Saltzman and Darwin J. Garringer
Flight Research Center

SUMMARY

Full-scale power-off flight lift and drag characteristics of the X-15 airplane are summarized for Mach numbers from 0.65 to 6.0 and for free-stream Reynolds numbers from 0.2×10^6 to 2.8×10^6 per foot. Comparisons are made between flight results and the wind-tunnel data that most nearly simulate the full-scale flight conditions.

Analysis of the results shows that 95 percent of the maximum supersonic lift-drag ratio can be obtained over an angle-of-attack range from about 7° to 12° . Thus, a near-optimum post-burnout gliding range can be approximated by flying within this angle-of-attack band throughout the supersonic speed range.

There is a strong tendency toward uniformity of pressures over adjacent base surfaces, even at low supersonic speeds, despite great differences in forebody geometry. This tendency prevails for gliding flight as well as when the propulsive jet exhausts from the base region.

The apparent effect of a sting support on the base pressure of an X-15 wind-tunnel model was propagated onto the vertical-fin base at least one sting diameter above and about one-half sting diameter forward of the sting-model intercept at Mach numbers between 2.5 and 3.5. That is, the sting effect was propagated significantly beyond the fuselage base annulus. For the X-15, this effect amounts to from 8 to 15 percent of the base drag between these Mach numbers. For some future vehicles and missions, proper accounting of this interference effect may be necessary to adequately predict the full-scale transonic and supersonic performance.

Specially conducted wind-tunnel-model drag studies, when extrapolated to full-scale Reynolds numbers by the T' (reference temperature) method, accurately predicted the full-scale zero-lift drag minus base drag of the X-15 at Mach numbers of 2.5 and 3.0.

The trimmed drag-due-to-lift factor is 43 percent higher than the inverse of the lift-curve slope $\frac{1}{C_{L\alpha}}$ at a Mach number of 5. The major part of this difference represents the relatively large component of trim drag that accompanies the X-15 configuration.

INTRODUCTION

The X-15 airplane is a unique research facility that provides full-scale aerodynamic data throughout a Mach number range extending from landing velocities to six times the speed of sound. The full-scale drag characteristics of the X-15 have been measured throughout much of this speed range and are reported in references 1 to 3. Reference 3 includes drag results up to the highest velocities attained; however, these data are limited and provide only a cursory examination of the drag characteristics at high Mach numbers.

Additional and more detailed information on the high-speed drag of the X-15 is presented herein. The previously reported results are included in order to make a relatively complete set of power-off drag polars available in one report. Comparisons are made between full-scale flight data and wind-tunnel tests that most nearly simulate the full-scale flow conditions and geometry.

The data presented were obtained from flight tests conducted at the NASA Flight Research Center, Edwards, Calif., on two X-15 airplanes that are essentially aerodynamically identical. Flight Mach numbers varied from about 0.65 to 6.0, and free-stream Reynolds numbers ranged from 10×10^6 to 140×10^6 , based on fuselage length. The flights considered were made from late 1959 to mid-1963.

SYMBOLS

A	aspect ratio
A_b	base area, ft^2
A_c	cross-sectional area, ft^2
a_z	measured longitudinal acceleration (along aircraft reference axis), g units
a_n	normal acceleration (load factor), g units
C_D	drag coefficient, $\frac{D}{qS}$
C_{D_b}	base-drag coefficient, $\frac{D_b}{qS}$
$(C_{D_{SB}})'$	speed-brake drag coefficient based upon frontal area (13.8 ft^2) of deflected speed brake
ΔC_D	increment in drag coefficient (reference area S)

$\frac{\Delta C_D}{\Delta C_L^2}$	drag-due-to-lift factor
C_L	lift coefficient, $\frac{L}{qS}$
$C_{L\alpha}$	slope of the lift curve with respect to α , deg^{-1} or rad^{-1}
C_{Pb}	base-pressure coefficient, $\frac{P_b - P}{q}$
c	chord length, ft
D	drag force along flight path, lb
g	gravitational acceleration, ft/sec^2
h	diameter or thickness of a base, ft
L	lift force normal to the flight path, lb
l	length, ft
M	free-stream Mach number
p	free-stream static pressure, lb/ft^2
P_b	base static pressure, lb/ft^2
q	free-stream dynamic pressure, $0.7M^2p$, lb/ft^2
R	free-stream Reynolds number, $\frac{Vl\rho}{\mu}$
S	wing area, ft^2
T_{ad}	adiabatic-wall temperature, $^{\circ}\text{R}$
T_w	wall temperature, $^{\circ}\text{R}$
V	true airspeed, ft/sec
W	airplane weight, lb
α	angle of attack, deg
Δ	error in corresponding parameter when used as a prefix for M , W , a_l , α , a_n , p , and V

δ	boundary-layer thickness, ft
ϵ	error in angle of attack caused by upwash, deg
μ	absolute viscosity, lb-sec/ft ²
ρ	air density, slugs/ft ³

Subscripts:

b	base
max	maximum
min	minimum
SB	speed brake
0	zero lift

AIRPLANE

The X-15 is a single-place, low-aspect-ratio monoplane (fig. 1) designed for aerodynamic and structural research at velocities up to six times the speed of sound. Because the X-15 is a rocket-powered aircraft, which must carry both fuel and oxygen in its tanks, the propellant volume is correspondingly limited. Therefore, the design performance ($M \approx 6$) is achieved by launching the X-15 from a modified B-52 airplane at an altitude of about 45,000 feet and a Mach number of 0.8.

For its earliest flights, the X-15 was powered by two four-chamber rocket engines (LR11) with a combined thrust of approximately 16,000 pounds for the major part of the powered trajectory. This installation provided about 4 minutes of powered flight and a maximum Mach number somewhat greater than 3. In 1960, a large single-chamber rocket engine (LR99) was installed that provides approximately 58,000 pounds of thrust for most of the powered trajectory. At this thrust level, the fuel is exhausted in about 85 seconds and a maximum Mach number of 6 can be achieved.

The configuration in which the two LR11 powerplants were used is referred to herein as the interim configuration, and the configuration with the large single-chamber LR99 engine is designated the basic configuration. The installation of the LR99 engine increased the fuselage base area by about 10 percent. Closeup views of the aft portions of each configuration are shown in figures 2(a) and 2(b).

Photographs of the airplane in the basic and the interim configurations are shown in figures 3(a) and 3(b), respectively. As can be seen, a slender airspeed boom-vane system was used in the interim configuration to obtain Mach number and flow direction. A spherical flow-direction sensor was used for the

basic configuration. This sensor, commonly termed the "ball nose," replaced the boom and vane system at the higher Mach numbers where aerodynamic heating can affect the reliability of vane nulling. Closeups of the vane-boom and ball-nose systems are shown in figures 4(a) and 4(b), respectively.

Detailed physical characteristics of the X-15 airplane in the basic configuration are presented in table I, and the cross-sectional area distribution of each configuration is shown in figure 5.

INSTRUMENTATION

Interim Configuration

For the flights made with the interim configuration, standard NASA internal-recording instruments were used to measure quantities pertinent to the definition of lift and drag (ref. 4). Accelerometers were positioned as close to the airplane center of gravity as practical, and corrections were made to compensate for any remaining displacement. Free-stream impact and static pressures were surveyed from nose-boom stations 71 inches and 63 inches, respectively, ahead of the intersection of the airplane nose and the boom. Angle of attack, which was measured by a floating vane about 43 inches forward of this intersection, was corrected for the effects of pitching velocity and inertia bending of the boom. Corrections for boom bending caused by airloads were found to be negligible.

The base-pressure instrumentation consisted of a standard NASA 24-cell photorecording manometer. Details on orifice locations are given in reference 5.

Basic Configuration

The instrumentation for the basic configuration remained essentially the same as for the interim configuration except that angle of attack and angle of sideslip were obtained from the ball nose, and Mach number and ambient pressure were obtained by means of radiosonde balloons and radar tracking of the aircraft. The method used to obtain Mach number and static pressure is discussed in detail in reference 6.

Base pressure was measured by a standard NASA 12-cell photorecording manometer. Details on orifice locations are included in reference 5.

METHOD

The accelerometer method, which is described in reference 4, was used to determine lift and drag. For power-off conditions, the following relationships apply:

$$C_L = \frac{Wa_n}{qS} \cos \alpha - \frac{Wa_l}{qS} \sin \alpha$$

$$C_D = \frac{Wa_l}{qS} \cos \alpha + \frac{Wa_n}{qS} \sin \alpha$$

ERROR AND RELIABILITY

Estimated Error in Drag

The following table shows the estimated maximum errors contributed by several sources to the drag coefficient for the boom-vane system at a Mach number of 3 and the ball-nose system at a Mach number of 5. The dynamic pressure for each example is 500 lb/ft².

Boom-vane system (M = 3)		Ball-nose system (M = 5)	
Error source	$\frac{\Delta C_D}{C_D}$, percent	Error source	$\frac{\Delta C_D}{C_D}$, percent
$\Delta M = \pm 0.03$	1	$\Delta p = \pm 1.5 \text{ lb/ft}^2$	5
$\Delta W = \pm 300 \text{ lb}$	2	$\Delta V = \pm 50 \text{ ft/sec}$	2
$\Delta a_l = \pm 0.005g$	1.3	$\Delta W = \pm 300 \text{ lb}$	2
$\Delta \alpha = \pm 0.5^\circ$	2	$\Delta a_l = \pm 0.005g$	2
$\Delta a_n = \pm 0.03g$	0.7	$\Delta \alpha = \pm 1.0^\circ$	4
		$\Delta a_n = \pm 0.03g$	1

The errors listed in the table above tend to be random, both in magnitude and sign, up to the values shown. Thus, it is obvious that the net error is

Flight condition	$\frac{\Delta C_D}{C_D}$, percent	
	Boom-vane system (M = 3)	Ball-nose system (M = 5)
C_{D0}	± 3	± 6
$(L/D)_{\max}$	± 4	± 7

not the absolute sum of the numbers shown but is the algebraic sum of numbers which range somewhat randomly within the limits given. On this basis, the table on the left is included to show the error that is believed to apply for faired values of drag coefficient, for a dynamic pressure of 500 lb/ft². This value of dynamic pressure is used because it represents a nominal

value for the range in which drag data were obtained. At higher dynamic pressures, the percentage error in drag coefficients would be less and, at lower dynamic pressures, the percentage error would be larger. It should be noted

that drag parameters derived from drag data faired with respect to Mach number have a smaller error than noted for the specific Mach numbers.

Angle-of-Attack Measuring Systems

The boom-vane and ball-nose angle-of-attack systems are each subject to upwash. Inasmuch as the orifices of the ball nose are much closer to the X-15 forebody than the angle-of-attack vane, this system should be affected more by upwash than the nulling vane of the boom-vane system. The large differences in subsonic lift-curve slope obtained by the two systems substantiate this assumption (see DISCUSSION OF RESULTS).

Experience with a similar boom-vane system on a YF-102 airplane (ref. 7) provided angle-of-attack values accurate to about $\pm 0.25^\circ$. Figures 6(a) and 6(b) show that the subsonic upwash of the X-15 and the YF-102 boom, fuselage, and wing calculated by the methods of references 8 and 9 is of approximately the same magnitude. These theoretical values of upwash are compared in order to demonstrate that the upwash experienced by the angle-of-attack vane on the X-15 should be no greater (theoretically, slightly less) than on the YF-102, which, as previously indicated, was very small. Therefore, on the basis of the favorable flight experience reported in reference 7, the theoretical correspondence shown in figure 6, and the wind-tunnel assessment of such boom-vane systems in reference 10, the boom vane is regarded as the most reliable system for the X-15 at subsonic and transonic speeds.

The estimated maximum error in angle of attack assigned the X-15 boom-vane system (0.5°) exceeds the error observed for the YF-102 experiment of reference 7 (0.25°), in which the data were obtained from selected maneuvers, and procedural errors and tare effects were minimized. Unfortunately, such care could not be exercised for many X-15 flights, and a larger maximum error must be assumed in making an error analysis for this paper.

The estimated maximum error in angle of attack assigned the ball-nose system ($\pm 1.0^\circ$) is also much larger than the design specification for nulling error¹ of the ball sensor ($\pm 0.1^\circ$), obtained from reference 11. The estimated maximum error is assigned to account for recorder-system error and procedural errors which, for these data, could not be defined with certainty.

TEST CONDITIONS

The drag data presented in this paper represent gliding flight (i.e., the rocket engine was not burning). Data were obtained during gradual push-down and pull-up maneuvers. The maximum range of angle of attack was from near 0° to 25° , and angle of sideslip was maintained at negligible values. The lower jettisonable fin was attached for all flights, and the configuration was clean except where it is indicated that the speed brakes were deflected. Mach

¹Nulling error is the limit of the sensor's ability to point at the local stagnation streamline and, hence, does not include recorder error.

number ranged from about 0.65 to 6.0 and free-stream Reynolds number varied from 0.2×10^6 to 2.8×10^6 per foot. Center-of-gravity position varied between 17 percent and 23 percent of the mean aerodynamic chord. For the interim configuration, the center of gravity was normally nearer the high end of this range; for the basic configuration it was usually nearer the low end. The data in this paper were chosen for conditions of zero or very low values of pitching acceleration. Experience has shown that, when these conditions are maintained, the flight-measured drag represents trimmed conditions.

DISCUSSION OF RESULTS

The basic flight data of this study are presented in figures 7(a) to 7(f), in which lift coefficient is plotted as a function of angle of attack and drag coefficient. The data for a given Mach number were, in many cases, obtained from more than one flight. The Mach number variation within a polar is much smaller at the lower Mach numbers than at the higher values. Most of the subsequent summary figures of flight data are derived from these basic data.

Lift-Curve Slope

The slope of the lift curve Cl_α is shown in figure 8 as a function of Mach number for lift coefficients ranging from the lowest values obtained to near maximum lift-drag ratio. The slope from the basic configuration in which angle of attack was derived from the ball nose is significantly lower than that from the interim boom-vane configuration at transonic and subsonic speeds. These ball-nose data are not included in figure 7. Both configurations experience upwash effects; however, for the reasons noted in the ERROR AND RELIABILITY section, the slopes derived from the boom-vane system are considered to be the more reliable values at the subsonic and transonic speeds. At the higher Mach numbers, the ball nose is used to obtain angle of attack for the basic configuration.¹

Values of lift-curve slope obtained from wind-tunnel models of the final X-15 configuration are also shown in figure 8. These data, obtained from references 14, 15, and 16, have been adjusted to trim about the 20-percent mean-aerodynamic-chord location as well as locations of ± 4 -percent mean aerodynamic chord from the 20-percent mean-aerodynamic-chord position. The model data shown in figure 8 are, consequently, presented as an increment which represents the spread in lift-curve slope caused by a corresponding shift of ± 4 -percent mean aerodynamic chord in the center-of-gravity position from the median

¹The results of reference 12 in conjunction with unpublished wind-tunnel data indicate that forebody upwash and lip effects on the ball-nose performance are negligible above $M = 1.8$. Reference 13 provides additional information on the ball-nose and nose-boom sensors. The study compares the in-flight performance of the ball-nose sensor with X-15 wind-tunnel studies, which include an early X-15 configuration at subsonic Mach numbers.

position. This shift is slightly greater than was actually experienced from flight-to-flight with the full-scale airplane.

The primary purpose of the wind-tunnel tests was to define the stability and control characteristics of the airplane, as opposed to a detailed lift and drag analysis. Consequently, interpolation over a considerable range of lift coefficient was required to derive the slope values shown. The flight (faired curve) and model results compare well at supersonic speeds in spite of the interpolation.

Drag

Figure 9 shows power-off drag coefficient as a function of Mach number for lift coefficients from 0 to 0.6. These curves were derived by cross-plotting the drag polars of figure 7. The drag for zero lift increases about twofold in traversing the transonic drag rise. A significant part of the zero-lift drag is base drag at the lower supersonic Mach numbers, and the steady decrease in zero-lift drag as Mach number is increased is caused primarily by the decay of base drag. The rapid increase in drag with lift is evident from the distribution of the lift coefficients.

A more graphic example of the drag-due-to-lift is shown in figure 10 for the interim configuration and the basic configuration. The primary cause of the displacement of these curves is believed to be differences in center-of-gravity location, which require a different horizontal-stabilizer position to maintain a given lift coefficient. The model data of reference 14 indicate that a 4-percent shift in center-of-gravity position would approximate this displacement, which amounts to about a 10-percent change in drag-due-to-lift factor at $M = 3.0$. The lift range considered in deriving the drag-due-to-lift factor extends from zero to the region in which $(L/D)_{\max}$ is obtained. The corresponding drag-due-to-lift data of reference 3 were based on relatively limited flight experience and failed to discriminate between the two configurations in terms of drag-due-to-lift.

Included in figure 10 are values for $\frac{1}{\pi A}$ and $\frac{1}{C_{L\alpha}}$ which correspond to theoretical limits of the drag-due-to-lift factor for fully developed and zero leading-edge suction, respectively, without regard for trim. At subsonic speeds, the measured drag-due-to-lift factor is closest to the zero suction level, as would be expected for a configuration with a predominant body and small, thin wings. At supersonic speeds, the measured drag-due-to-lift factor is significantly higher than $\frac{1}{C_{L\alpha}}$, which is often used as an approximation for untrimmed drag-due-to-lift. At $M = 5$, for example, $\frac{\Delta C_D}{\Delta C_L^2}$ is 43 percent higher than $\frac{1}{C_{L\alpha}}$. Most of this difference is attributable to high trim drag. This observation is supported by wind-tunnel data wherein $\frac{\Delta C_D}{\Delta C_L^2} \approx \frac{1}{C_{L\alpha}}$ for zero

stabilizer position, but, for trim, $\frac{\Delta C_D}{\Delta C_L^2}$ was much the larger ($M = 3$, ref. 14).

Values of drag-due-to-lift factor obtained from wind-tunnel-model tests (refs. 14, 15, and 16) are also included in figure 10. These data are derived from the same tests as the model lift-curve-slope data of figure 8 and are plotted in a similar manner so that the effect of a ± 4 -percent shift in center-of-gravity position may be seen. The resulting change in the amount of horizontal-stabilizer deflection required for trim has a large effect on drag-due-to-lift factor at supersonic speeds as compared to the influence observed on the lift-curve slopes of figure 8.

This sensitivity to center-of-gravity location, which is evident for both the full-scale and the model results, emphasizes that much attention should be devoted to trim characteristics and control of center-of-gravity position during the early design and wind-tunnel-model testing of short-coupled supersonic and hypersonic aircraft.

An attempt was made to estimate the X-15 trim drag by analytical methods in reference 3. It was found that both supersonic and hypersonic theory significantly underestimated the stabilizer deflection required for trim. This discrepancy was a result of the complex flow field in which the horizontal stabilizer is immersed, even at low deflection angles, complicated further by the large gap which occurs along the inboard edge of the stabilizer as deflection angles become large.

Lift-Drag Ratio

The rather significant increase in the drag-due-to-lift factor with Mach number would result in a steadily deteriorating $(L/D)_{\max}$ curve for an airplane with more conventional afterbody geometry than the X-15. The high transonic base drag of the X-15, caused by the large blunt base, reduces with Mach number as the drag-due-to-lift increases. The net result is an $(L/D)_{\max}$ curve that is depressed by base drag at the lower supersonic Mach numbers and by high drag-due-to-lift at the higher Mach numbers. The maximum lift-drag-ratio curve is, thus, relatively insensitive to Mach number throughout the supersonic speed range. This insensitivity is shown in figure 11, in which the level of $(L/D)_{\max}$ throughout the higher speeds is within 12 percent of the value at $M = 1.5$. The decrement in maximum lift-drag ratio associated with the transonic drag rise is about one-third of the subsonic value of $(L/D)_{\max}$.

Figure 12 shows the lift coefficient and angle of attack needed to achieve $(L/D)_{\max}$ as Mach number is varied. The lift coefficient required varies over a threefold range; however, the corresponding angle of attack is relatively invariant through the supersonic Mach number.

Figure 13(a) shows the relatively flat-topped variation of lift-drag ratio with angle of attack for two selected Mach numbers. The ticks on the curves indicate the range of angle of attack within which 95 percent of the maximum lift-drag ratio can be obtained. The shaded area in figure 13(b) represents

the range of angle of attack that can be flown throughout the Mach number range, while still obtaining 95 percent of $(L/D)_{\max}$. Thus, for the X-15, a near-optimum post-burnout gliding range can be approximated by flying at any angle of attack between about 7° and 12° throughout the entire supersonic speed range. This feature is characteristic, of course, of aircraft that have a low value of maximum lift-drag ratio.

Base Drag

As mentioned earlier, the shape of the X-15 lift-drag-ratio curve is dependent on the decay of base drag with Mach number. Base-drag coefficient as a function of Mach number is shown in figure 14(a). These data are derived from the base-pressure data presented in reference 5. The short-dashed lines in the transonic region do not represent base-drag-coefficient levels but merely serve to connect the subsonic data with the supersonic data for a given base component. The long-dashed curve shows the ratio of base drag to zero-lift drag as a function of Mach number. The effect of base drag on the terminal-phase performance of a blunt-base reentry vehicle or boost-glide aircraft may be large because, as shown in the figure, base drag becomes a dominant factor at subsonic and low supersonic speeds and is significant even at $M = 6$.

Figure 14(b) shows the base-drag increment per unit area for the vertical fins (the base being preceded by short quasi-two-dimensional surfaces) and for the side fairing (in this instance, preceded by much longer quasi-three-dimensional surfaces). The base-drag-coefficient increments per unit of area are nearly equal, even at the lower speeds where flow phenomena normally discriminate between two-dimensional and three-dimensional shapes. This condition is not consistent with body-of-revolution and wing or wedge turbulent-flow base-drag results obtained separately (refs. 17 and 18). The side fairing, of course, is not a body of revolution. The shape of this base and the fact that it is preceded by a long flow length $\left(\frac{l}{h} \approx 23\right)$ accompanied by a relatively thick boundary layer $\left(\frac{\delta}{h} \approx 0.3\right)$ suggest that its base-pressure (drag) characteristics would approach those of a body of revolution. Therefore, representative values of two- and three-dimensional base-drag increments from reference 17 are included in figure 14(b) to illustrate how far the side-fairing values depart from body-of-revolution levels. The observation that the drag increments per unit area are similar for the fin and the side-fairing bases is consistent with the results of reference 5. In that study, the "dead air" region behind the large base components was found to serve as an effective channel for equalizing the pressure over the bases during rocket-engine operation as well as during gliding flight. Apparently, for large adjacent base areas, there is a strong tendency toward uniformity of pressure over the several bases, despite great differences of forebody geometry, even at relatively low supersonic speeds.

The almost complete dependence of the shape of zero-lift drag upon the variation of base drag is shown in figure 15. The increment of drag separating the two curves is, of course, composed primarily of wave and friction drag.

Comparison of Flight and Wind-Tunnel Minimum Drag ($C_{D0} - C_{Db}$)

Friction drag, per se, cannot be readily defined for the X-15; however, an assessment of the effect of Reynolds number on friction drag is reported in reference 3. The results of the assessment are shown in figures 16(a) and 16(b) as the variation of zero-lift drag minus base drag with Reynolds number. The experimental data for low Reynolds numbers are represented by 1/15-scale wind-tunnel-model results; the interim-configuration X-15 provided the full-scale Reynolds number data. For the Mach numbers considered, the T' method of references 19 and 20 provided a satisfactory extrapolation of wind-tunnel drag to the full-scale Reynolds numbers.

For these extrapolations, using the T' method, the recovery temperature was assumed to be that for an adiabatic, smooth, flat plate with a turbulent boundary layer and a recovery factor of 0.88. The skin temperatures on the X-15 are not in equilibrium, however. Thus, at the full-scale Reynolds number and $M = 3$, a calculated increment of skin-friction-drag coefficient was included corresponding to the minimum temperature measured on the aft fuselage ($T_{ad} = 538^\circ \text{ F}$ and $(T_w)_{\min} = 100^\circ \text{ F}$). Therefore, the most exact extrapolation from the model Reynolds numbers to full scale would result in a value between the calculated levels for T_{ad} and $(T_w)_{\min}$. For these extrapolations it was assumed that wave drag did not vary with Reynolds number, in that boundary-layer-displacement effects are negligible on the X-15 configuration at Mach numbers up to 3.

It should be emphasized that the agreement shown in figure 16 was obtained through analysis of the optimum flight maneuvers and by means of specially conducted wind-tunnel tests in which axial force and dynamic pressure were the primary measurements. The wind-tunnel measurements were made on a precisely scaled model that included all of the protuberances on the airplane, such as exhaust ports, camera fairings, and antennae. Transition on the model was fixed near stations corresponding to those that experienced transition in full-scale flight, and the increment of drag attributable to the tripping device was subtracted.

In addition, it should be noted that the X-15 airplane and the model were both very rigid, thus circumventing flexibility problems and any subsequent effects on trim. Also, the X-15 has no leading-edge slats, spoilers, or hinged rudders that would add uncertainty because of possible leakage, to a comparison of model and full-scale results. Furthermore, there were no inlet airflows, propulsive jets, or bypass airflows to simulate on the model, and the problem of measuring thrust in flight was avoided by considering only gliding flight. Therefore, the comparison shown in figure 16 represents an experiment in which many of the complicating factors associated with flexible, air-breathing aircraft were avoided. Even under such favorable conditions, however, it was necessary to subtract the base drag from both the wind-tunnel-model and full-scale results because the model tests could not simulate the base component of drag.

The study of reference 3, in which the base drag of the model was carefully measured and subtracted, provides a unique opportunity to examine the extent of sting effects on base pressure. At least two sources of error are commonly recognized in the simulation of base drag from wind-tunnel tests of sting-supported models, assuming that the afterbody geometry is correct, the boundary-layer condition is known (i.e., turbulent or laminar), shock reflection from the tunnel wall has been avoided, and exhaust effects are excluded. One source of error would be the sting effect, and another would concern the boundary layer. For bodies with relatively high fineness ratios, the ratio of boundary-layer thickness to base diameter can become disproportionately large for models in comparison to that for full-scale flight conditions. This viscous effect can result in the boundary-layer-induced base-pressure discrepancy just mentioned. By comparing model and full-scale base-pressure results from the X-15 upper vertical fin, which is a low-fineness-ratio shape, the boundary-layer effect is greatly reduced and can be estimated. Thus, the remaining increment, which is believed to be primarily a sting effect, can be defined.

Figure 17 shows the pressure ratio $\frac{p_b}{p}$ from the upper vertical fin of the full-scale X-15 and the 1/15-scale model plotted against $\frac{c}{hR^{1/5}}$. The slopes of the curves extending from the flight data show the effect of boundary-layer thickness relative to base thickness, previously discussed. These curves were interpolated from the blunt-trailing-edge-wing data of reference 21. The values of $\frac{p_b}{p}$ for the model are much higher than the flight results adjusted to similar values of $\frac{c}{hR^{1/5}}$. The differences are believed to be primarily attributable to the sting, which intersects the model fuselage base about one-half sting diameter aft of the fin base and over 1 sting diameter below the center of the fin. The results show that the difference between the model and the flight pressure ratios increases with Mach number for these speeds, thus emphasizing that this probable sting interference should not be considered as only a transonic problem.

When $\frac{p_b}{p}$ is converted to an increment of base drag, or to pressure coefficient, the interference effect does not appear to be so large; for example, the effect is about 8 percent of the full-scale pressure coefficients at $M = 2.5$ and 15 percent at $M = 3.5$. This is the order of magnitude of discrepancies between model and flight results for the other components of base pressure on the X-15, as reported in reference 5. The supersonic flight and wind-tunnel data compiled in reference 5, from references 3, 14, 22, and 23, and transonic and subsonic results from reference 15 are shown in figures 18(a) to 18(c). The discussion concerning the vertical-fin base pressures (fig. 17), in conjunction with the relative uniformity of pressure level over the several adjacent base surfaces (page 11), suggests that the discrepancies shown in figure 18, for the several sources of data, are also primarily attributable to the sting. It is not intended to imply that this discrepancy between the model and full-scale data is particularly important to the X-15

airplane. It should be emphasized, however, that the discrepancy (probable sting interference) is not limited to the annulus region of the fuselage and that, for some future vehicles and missions, proper accounting of sting interference may be necessary.

Drag of the Speed Brakes

The full-scale flight and wind-tunnel values of drag increment for the X-15 speed brakes are shown in figure 19(a) for the brakes fully opened (35°). Figure 19(b) shows the ratio of the full-scale speed-brake-drag increment to the basic (clean configuration) zero-lift drag of the X-15. The drag contribution of the speed brakes is about 1.75 times the clean zero-lift drag of the airplane at subsonic speeds and about 1 to 1.5 times the clean zero-lift drag through the supersonic range, although the brake frontal area is only about 36 percent of the frontal area of the basic clean airplane.

The dashed curve of figure 19(b) shows the drag coefficient of the speed brakes based upon their frontal area, which is the conventional method of defining decelerator-drag coefficient. Also shown (shaded area) is the range of drag coefficients, obtained from the wind-tunnel tests of reference 24, for several typical "towed" decelerators. The towed-decelerator values represent shapes immersed in a symmetrical wake; therefore, it is uncertain to what extent these values are applicable to the X-15 wake. It is of interest to note, however, that the X-15 speed brakes compare favorably with towed decelerators as drag-producing devices. This comparison does not, of course, take into account the relative cost, in weight, of obtaining the respective deceleration drag-coefficient levels.

CONCLUSIONS

Analysis of the power-off, full-scale-drag characteristics of the X-15 airplane and comparison with wind-tunnel-model data have shown that:

1. The transonic drag-rise increment of the X-15 is about equal to the subsonic level of drag for zero lift.
2. Transonic drag rise reduces the maximum lift-drag ratio by one-third the subsonic value.
3. Ninety-five percent of the maximum supersonic lift-drag ratio can be obtained over an angle-of-attack range from about 7° to 12° . Thus, a near-optimum post-burnout gliding range can be approximated by flying within this angle-of-attack band throughout the supersonic speed range.
4. There is a strong tendency toward uniformity of pressures over adjacent base surfaces, even at low supersonic speeds, despite great differences in forebody geometry. This tendency prevails for gliding flight as well as when the propulsive jet exhausts from the base region.

5. The apparent effect of a sting support on the base pressure of an X-15 wind-tunnel model was propagated onto the vertical-fin base at least 1 sting diameter above and about one-half sting diameter forward of the sting-model intercept at Mach numbers between 2.5 and 3.5. That is, the sting effect was propagated significantly beyond the fuselage base annulus. For the X-15, this effect amounts to from 8 to 15 percent of the base drag between these Mach numbers. For some future vehicles and missions, proper accounting of this interference effect may be necessary to adequately predict the full-scale transonic and supersonic performance.

6. Specially conducted wind-tunnel-model drag studies when extrapolated to full-scale Reynolds numbers by the T' (reference temperature) method accurately predicted the full-scale zero-lift drag minus base drag of the X-15 at Mach numbers of 2.5 and 3.0.

7. The trimmed drag-due-to-lift factor is 43 percent higher than the inverse of the lift-curve slope $\frac{1}{C_{L\alpha}}$ at a Mach number of 5. The major part of this difference represents the relatively large component of trim drag that accompanies the X-15 configuration.

8. Trimmed values of lift-curve slope from full-scale flight and wind-tunnel models agree well at supersonic Mach numbers.

Flight Research Center,
National Aeronautics and Space Administration,
Edwards, Calif., October 15, 1965.

REFERENCES

1. Matranga, Gene J.: Analysis of X-15 Landing Approach and Flare Characteristics Determined From the First 30 Flights. NASA TN D-1057, 1961.
2. Saltzman, Edwin J.: Preliminary Full-Scale Power-Off Drag of the X-15 Airplane for Mach Numbers From 0.7 to 3.1. NASA TM X-430, 1960.
3. Hopkins, Edward J.; Fetterman, David E., Jr.; and Saltzman, Edwin J.: Comparison of Full-Scale Lift and Drag Characteristics of the X-15 Airplane With Wind-Tunnel Results and Theory. NASA TM X-713, 1962.
4. Beeler, De E.; Bellman, Donald R.; and Saltzman, Edwin J.: Flight Techniques for Determining Airplane Drag at High Mach Numbers. NACA TN 3821, 1956.
5. Saltzman, Edwin J.: Base Pressure Coefficients Obtained From the X-15 Airplane for Mach Numbers Up to 6. NASA TN D-2420, 1964.
6. Larson, Terry J.; and Webb, Lannie D.: Calibrations and Comparisons of Pressure-Type Airspeed-Altitude Systems of the X-15 Airplane From Subsonic to High Supersonic Speeds. NASA TN D-1724, 1963.
7. Saltzman, Edwin J.; Bellman, Donald R.; and Musialowski, Norman T.: Flight-Determined Transonic Lift and Drag Characteristics of the YF-102 Airplane With Two Wing Configurations. NACA RM H56E08, 1956.
8. Rogallo, Vernon L.: Effects of Wing Sweep on the Upwash at the Propeller Planes of Multiengine Airplanes. NACA TN 2795, 1952.
9. Yaggy, Paul F.: A Method for Predicting the Upwash Angles Induced at the Propeller Plane for a Combination of Bodies With an Upswept Wing. NACA TN 2528, 1951.
10. Richardson, Norman R.; and Pearson, Albin O.: Wind-Tunnel Calibrations of a Combined Pitot-Static Tube, Vane-Type Flow-Direction Transmitter, and Stagnation-Temperature Element at Mach Numbers From 0.60 to 2.87. NASA TN D-122, 1959.
11. Anon.: Q-Ball Airflow Direction and Air Data Sensors, General Descriptions. NORT 63-365, Nortronics, Div. of Northrop Corp., Oct. 1963.
12. Cary, John P.; and Keener, Earl R.: Flight Evaluation of the X-15 Ball-Nose Flow-Direction Sensor as an Air-Data System. NASA TN D-2923, 1965.
13. Wolowicz, Chester H.; and Gossett, Terrence D.: Operational and Performance Characteristics of the X-15 Spherical, Hypersonic Flow-Direction Sensor. NASA TN D-3070, 1965.

14. Franklin, Arthur E.; and Lust, Robert M.: Investigation of the Aerodynamic Characteristics of a 0.067-Scale Model of the X-15 Airplane (Configuration 3) at Mach Numbers of 2.29, 2.98, and 4.65. NASA TM X-38, 1959.
15. Osborne, Robert S.: Stability and Control Characteristics of a 0.0667-Scale Model of the Final Version of the North American X-15 Research Airplane (Configuration 3) at Transonic Speeds. NASA TM X-758, 1963.
16. Penland, Jim A.; and Fetterman, David E., Jr.: Static Longitudinal, Directional, and Lateral Stability and Control Data at a Mach Number of 6.83 of the Final Configuration of the X-15 Research Airplane. NASA TM X-236, 1960.
17. Love, Eugene S.: Base Pressure at Supersonic Speeds on Two-Dimensional Airfoils and on Bodies of Revolution With and Without Fins Having Turbulent Boundary Layers. NASA TN 3819, 1957. (Supersedes NACA RM L53C02.)
18. Hoerner, Sigward F.: Fluid-Dynamic Drag. Publ. by the author (148 Busted Drive, Midland Park, N. J.), 1958.
19. Sommer, Simon C.; and Short, Barbara J.: Free-Flight Measurements of Turbulent-Boundary-Layer Skin Friction in the Presence of Severe Aerodynamic Heating at Mach Numbers From 2.8 to 7.0. NACA TN 3391, 1955.
20. Bertram, Mitchel H.: Calculations of Compressible Average Turbulent Skin Friction. NASA TR R-123, 1962.
21. Chapman, Dean R.; Wimbrow, William R.; and Kester, Robert H.: Experimental Investigation of Base Pressure on Blunt-Trailing-Edge Wings at Supersonic Velocities. NACA Rep. 1109, 1952. (Supersedes NACA TN 2611.)
22. Leupold, Mathias J.; and Freeman, Elizabeth M.: A Second Series of Supersonic Force Tests on the Full-Span Model X-15 for North American Aviation Incorporated. WTR 200, Mass. Inst. of Tech. (Naval Supersonic Laboratory), Sept. 1958.
23. Franklin, Arthur E.; and Silvers, H. Norman: Investigation of the Aerodynamic Characteristics of a 0.067-Scale Model of the X-15 Airplane (Configuration 2) at Mach Numbers of 2.29, 2.98, 3.96, and 4.65. NASA MEMO 4-27-59L, 1959.
24. McShera, John T., Jr.: Aerodynamic Drag and Stability Characteristics of Towed Inflatable Decelerators at Supersonic Speeds. NASA TN D-1601, 1963.

TABLE I
PHYSICAL CHARACTERISTICS OF THE BASIC X-15 AIRPLANE

Wing -

Airfoil section	NACA 66005 (modified)	
Total area (includes 94.98 ft ² covered by fuselage), ft ²	200	
Span, ft	22.36	
Mean aerodynamic chord, ft	10.27	
Root chord, ft	14.91	
Tip chord, ft	2.98	
Taper ratio	0.20	
Aspect ratio	2.50	
Sweep at 25-percent-chord line, deg	25.64	
Incidence, deg	0	
Dihedral, deg	0	
Aerodynamic twist, deg	0	
Flap:		
Type	Plain	Plain
Area (each), ft ²	8.30	
Span (each), ft	4.50	
Inboard chord, ft	2.61	
Outboard chord, ft	1.08	
	Original	Present
Deflection, down (nominal design), deg	40	32
Ratio flap chord to wing chord		0.22
Ratio total flap area to wing area		0.08
Ratio flap span to wing semispan		0.40
Trailing-edge angle, deg		5.67
Sweepback angle of hinge line, deg		0

Horizontal tail -

Airfoil section	NACA 66005 (modified)	
Total area (includes 63.29 ft ² covered by fuselage), ft ²	115.34	
Span, ft	18.08	
Mean aerodynamic chord, ft	7.05	
Root chord, ft	10.22	
Tip chord, ft	2.11	
Taper ratio	0.21	
Aspect ratio	2.83	
Sweep at 25-percent-chord line, deg	45	
Dihedral, deg	-15	
Ratio horizontal-tail area to wing area	0.58	
Movable surface area, ft ²	51.77	
Deflection:		
Longitudinal, up, deg		15
Longitudinal, down, deg		35
Lateral differential (pilot authority), deg		±15
Lateral differential (autopilot authority), deg		±30
Control system	Irreversible hydraulic boost with artificial feel	

TABLE I.— Concluded

PHYSICAL CHARACTERISTICS OF THE BASIC X-15 AIRPLANE

Upper vertical tail —

Airfoil section	10° single wedge
Total area, ft ²	40.91
Span, ft	4.58
Mean aerodynamic chord, ft	8.95
Root chord, ft	10.21
Tip chord, ft	7.56
Taper ratio	0.74
Aspect ratio	0.51
Sweep at 25-percent-chord line, deg	23.41
Ratio vertical-tail area to wing area	0.20
Movable surface area, ft ²	26.45
Deflection, deg	±7.50
Sweepback of hinge line, deg	0
Control system	Irreversible hydraulic boost with artificial feel

Lower vertical tail —

Airfoil section	10° single wedge
Total area, ft ²	34.41
Span, ft	3.83
Mean aerodynamic chord, ft	9.17
Root chord, ft	10.21
Tip chord, ft	8
Taper ratio	0.78
Aspect ratio	0.43
Sweep at 25-percent-chord line, deg	23.41
Ratio vertical-tail area to wing area	0.17
Movable surface area, ft ²	19.95
Deflection, deg	±7.50
Sweepback of hinge line, deg	0
Control system	Irreversible hydraulic boost with artificial feel

Fuselage —

Length, ft	49.5
Maximum width, ft	7.33
Maximum depth, ft	4.67
Maximum depth over canopy, ft	4.97
Side area (total), ft ²	215.66
Fineness ratio	10.91

Speed brake —

Area (each), ft ²	5.37
Mean span (each), ft	1.60
Chord (each), ft	3.36
Deflection, deg	35
Frontal area at maximum deflection, ft ²	13.8

Base area (fuselage, side fairing, vertical fins, wings,
horizontal tail, landing skids), ft²

34.1

Total frontal area (maximum) including wing and horizontal
tail at 0° deflection angle, ft²

38.8

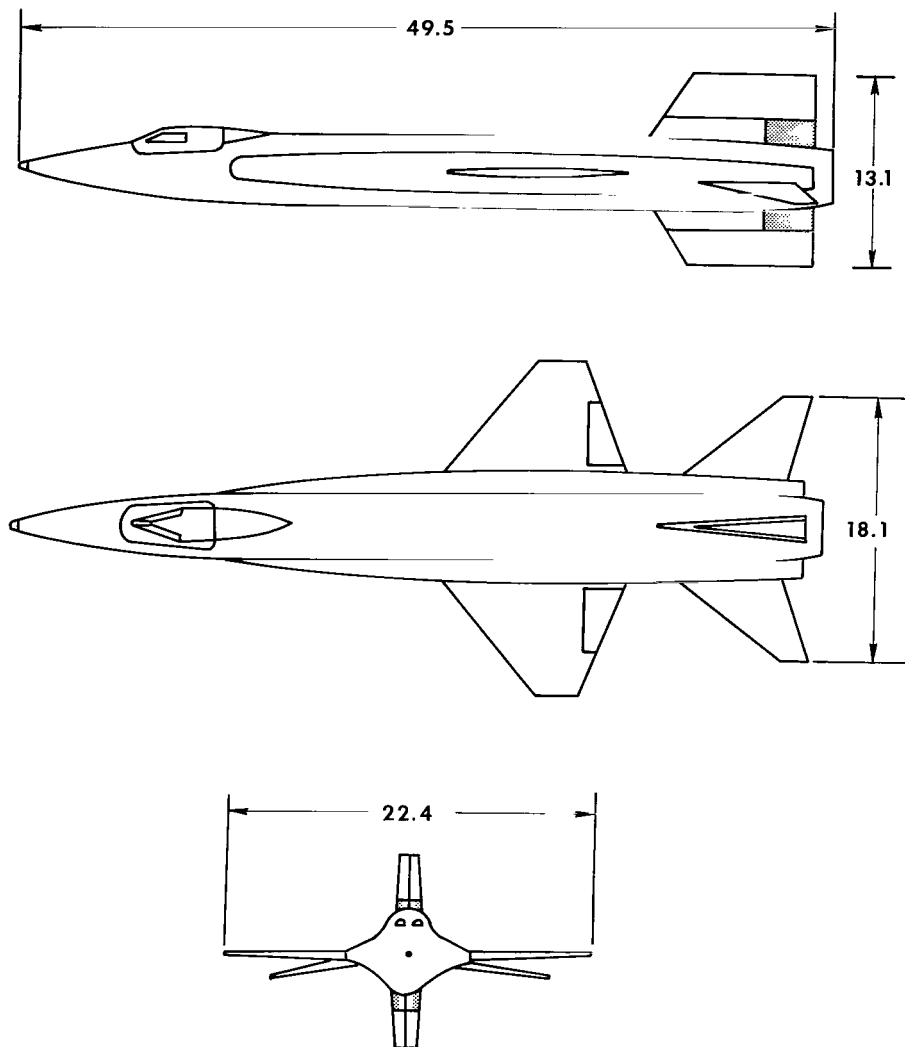
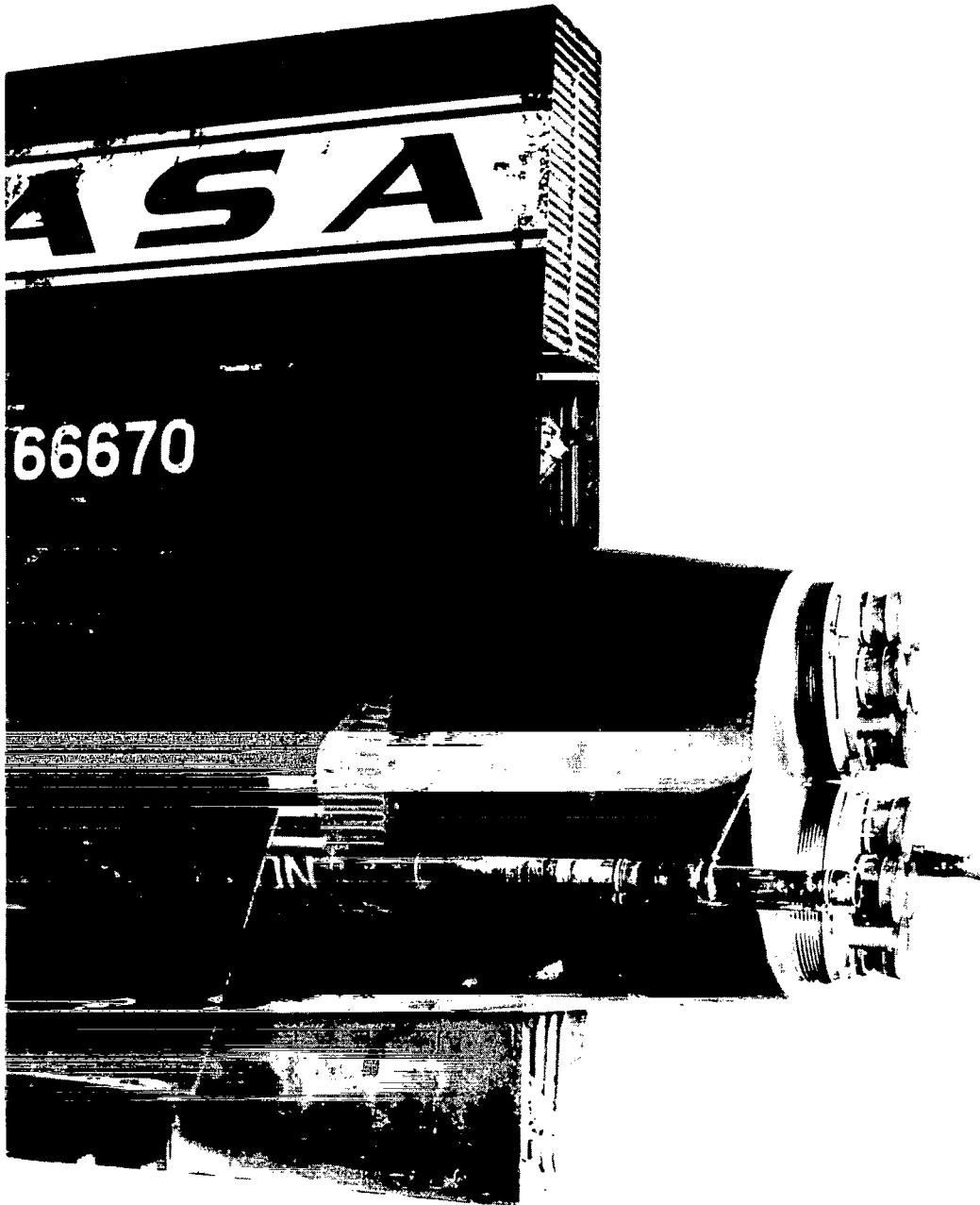


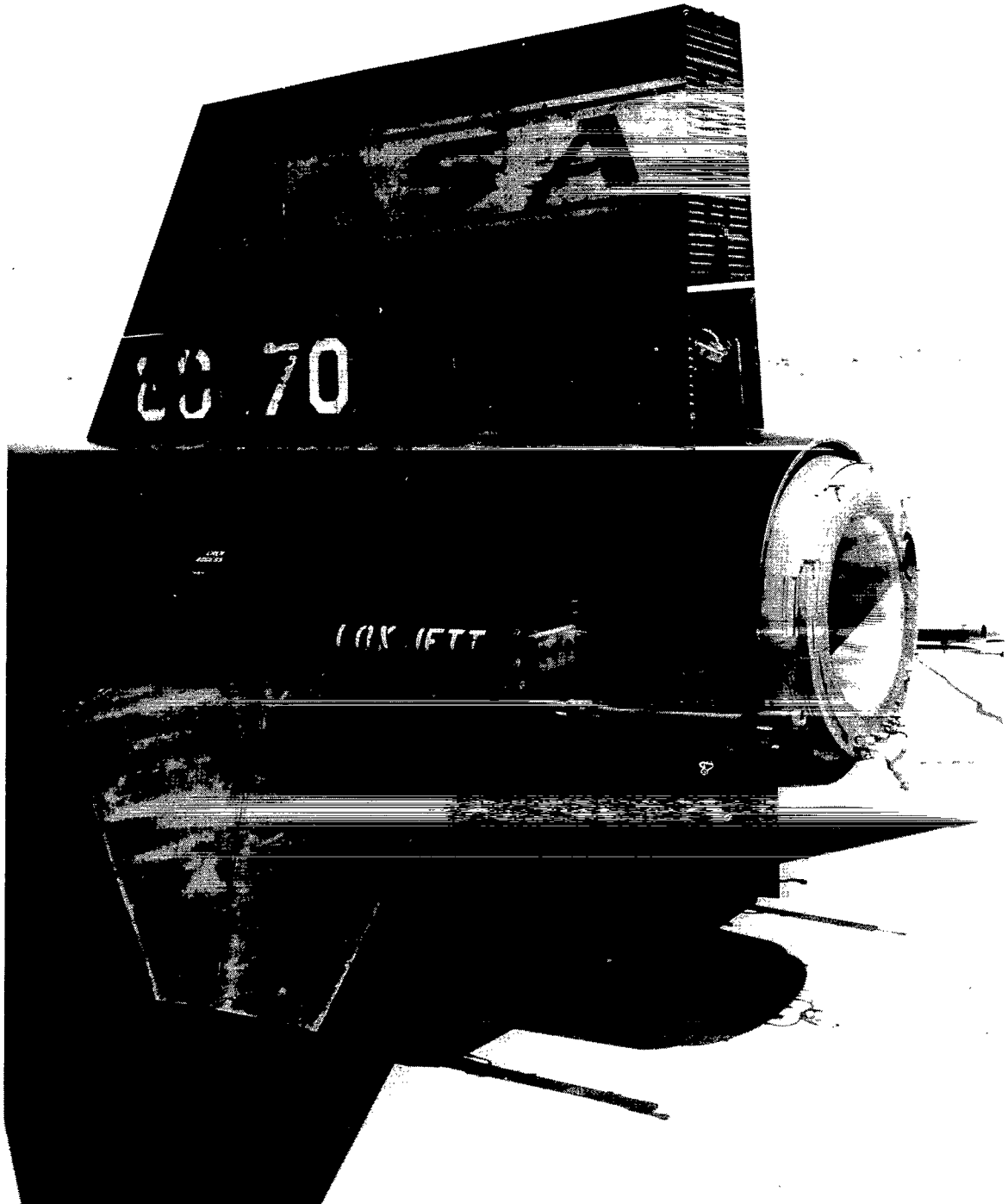
Figure 1.— Three-view drawing of the basic X-15 airplane. Shaded areas denote speed brakes. All dimensions in feet.



(a) Interim configuration.

E-6646

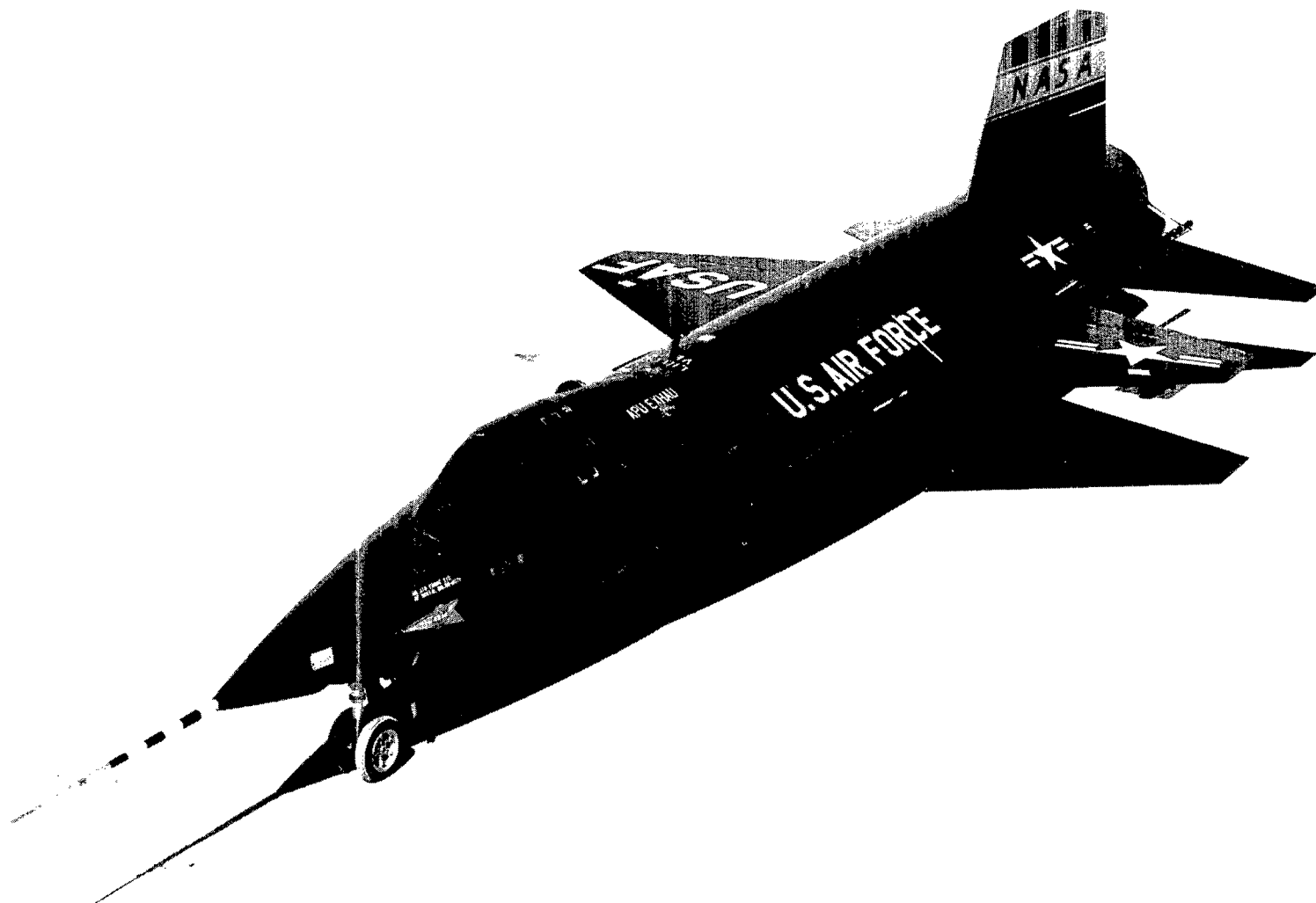
Figure 2.- X-15 viewed from the left rear. Lower jettisonable fin removed.



(b) Basic configuration.

E-9908

Figure 2.- Concluded.



(a) Interim configuration.

E-5251

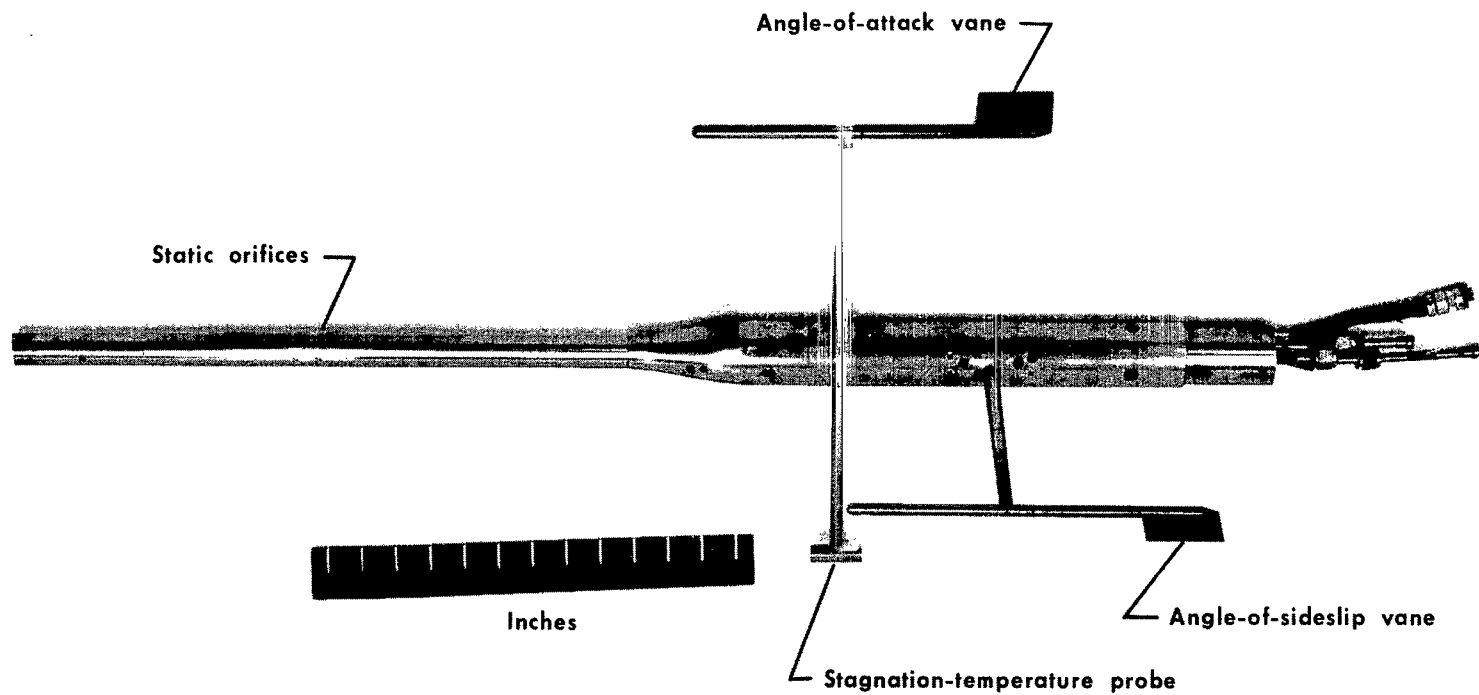
Figure 3.- X-15 airplane.



(b) Basic configuration.

E-7902

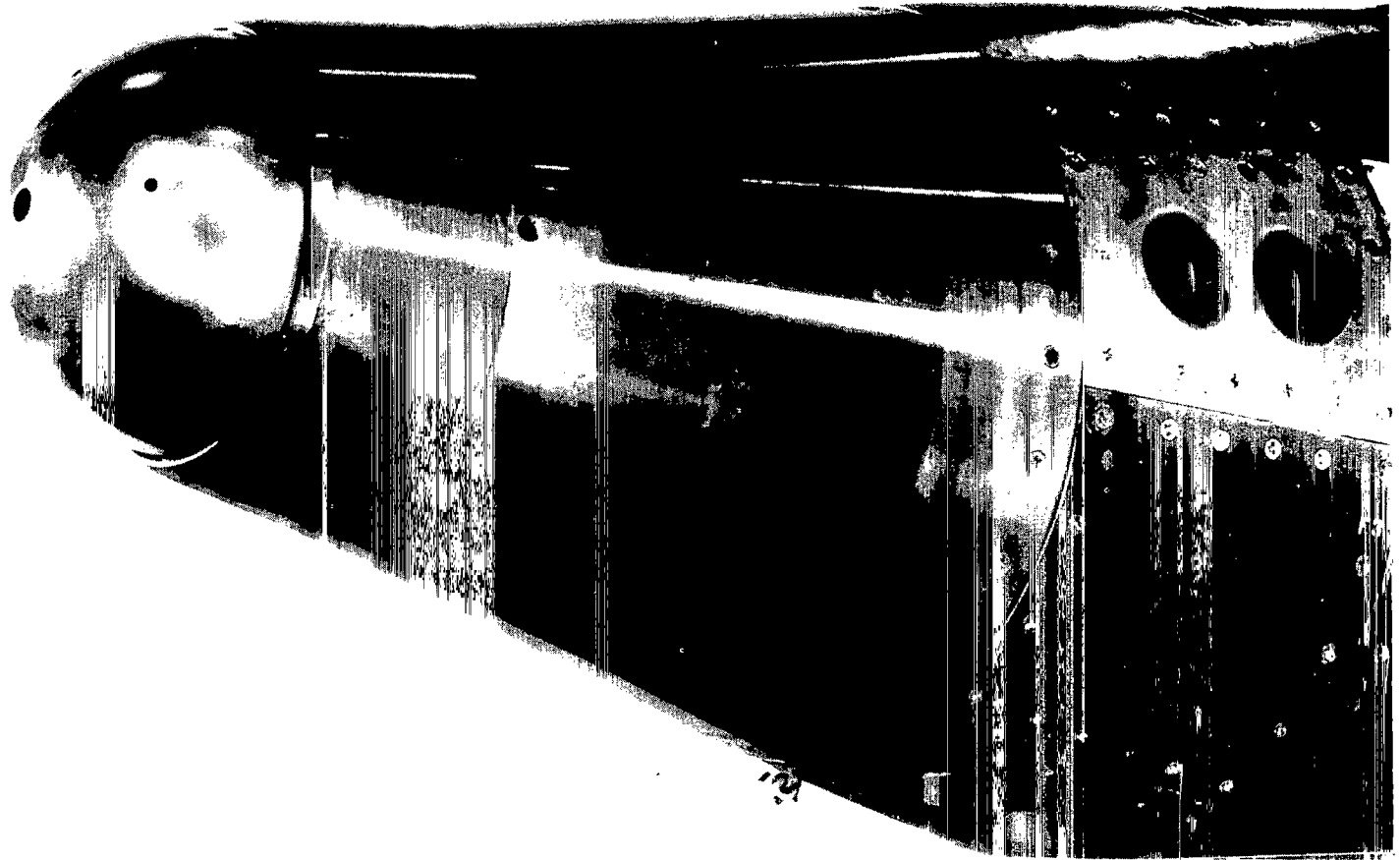
Figure 3.- Concluded.



(a) Interim configuration, vane-boom system.

E-13702

Figure 4.- Impact-pressure and flow-angle sensors.



(b) Basic configuration, ball-nose system.

ES-1385

Figure 4.- Concluded.

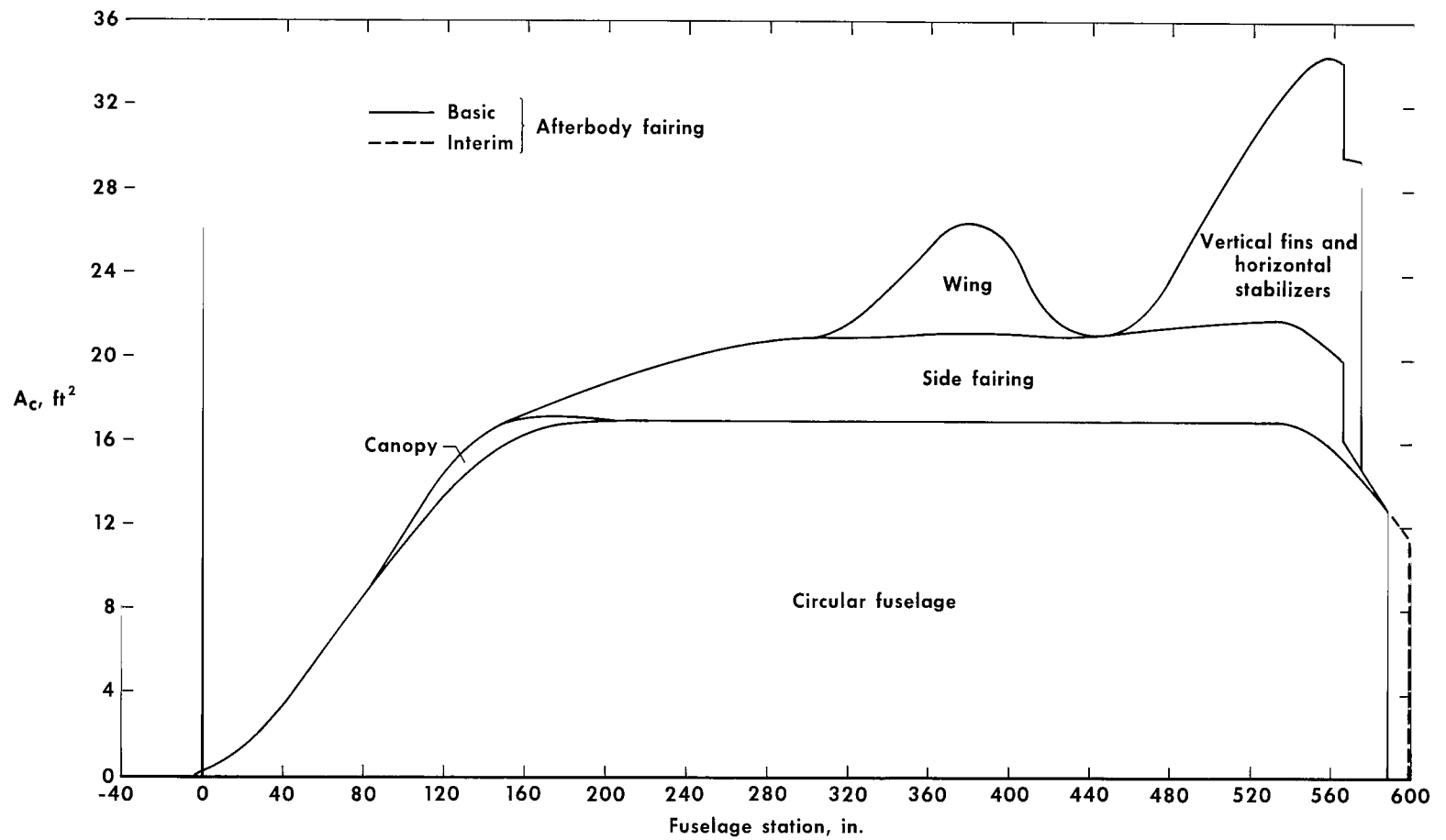
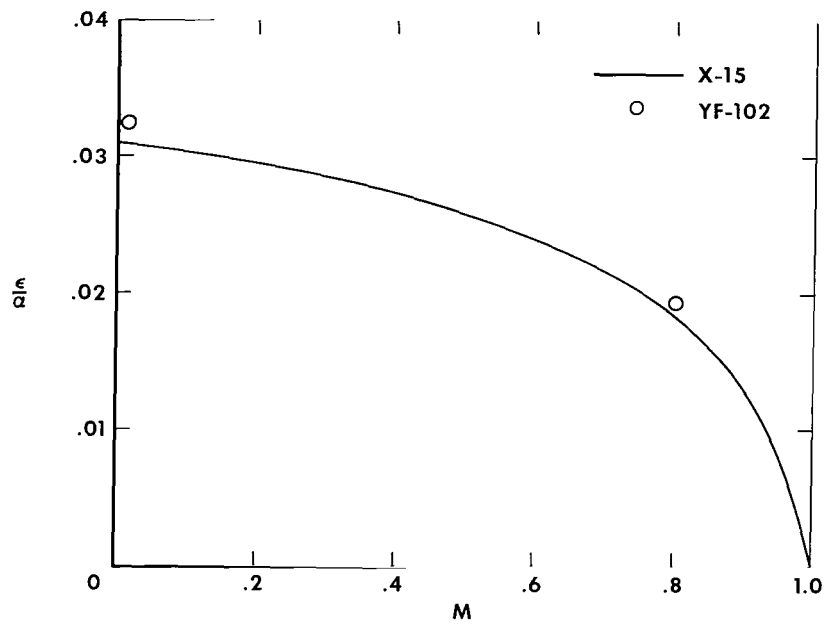
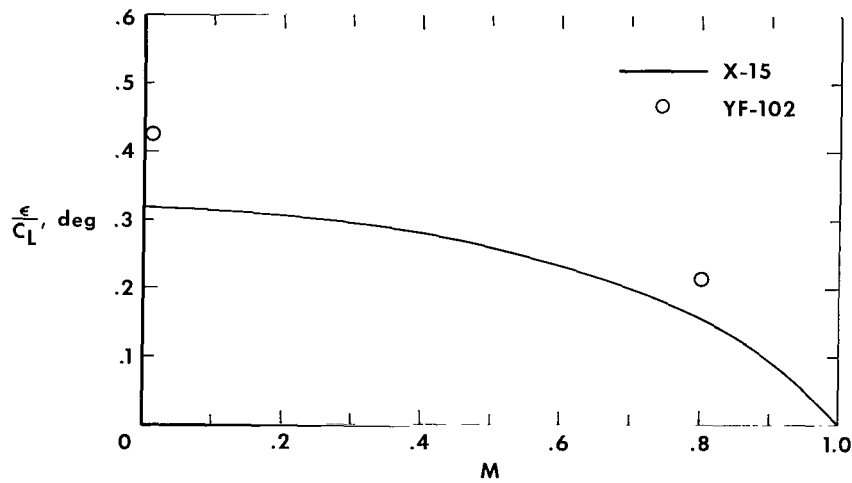


Figure 5.- X-15 area distribution.

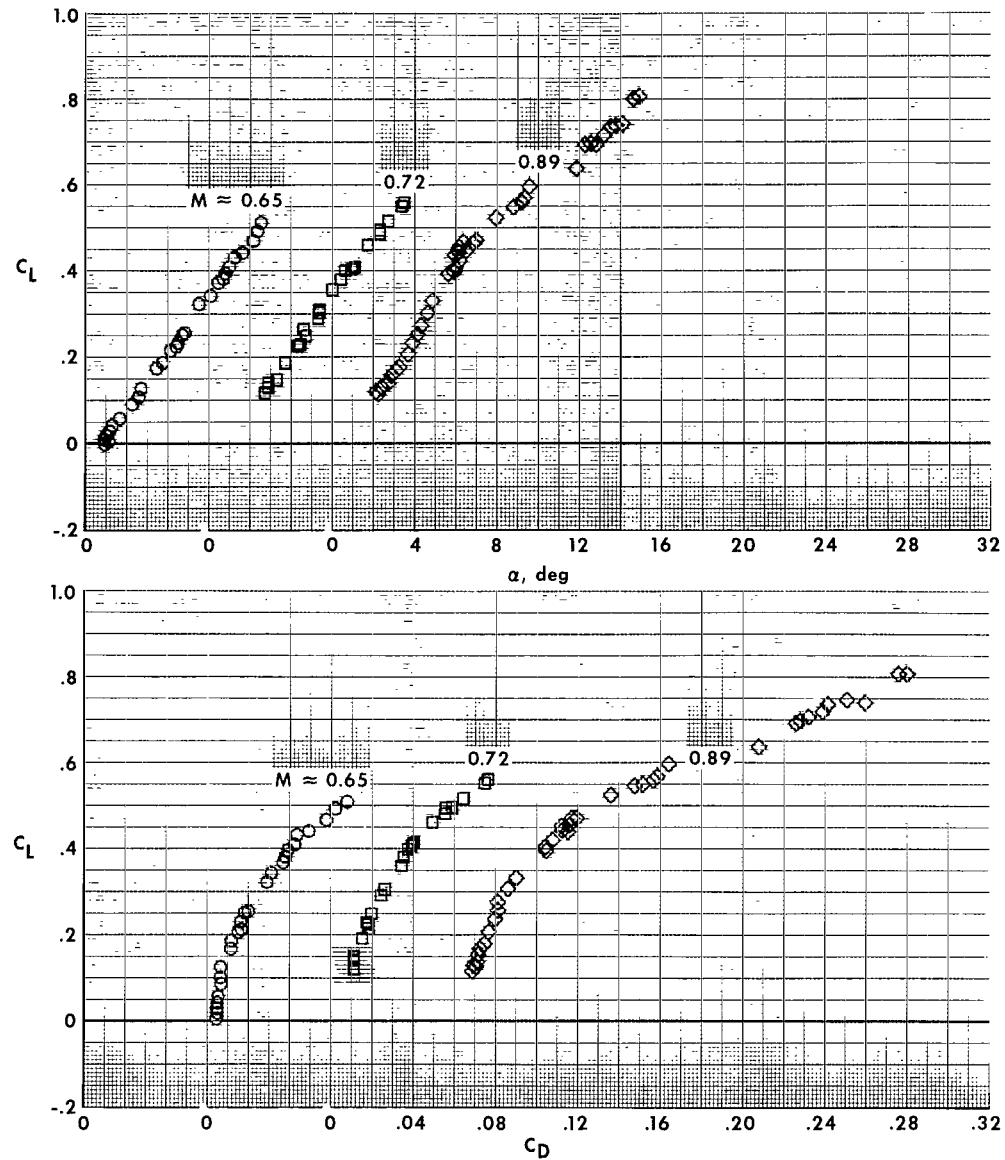


(a) Boom and fuselage.

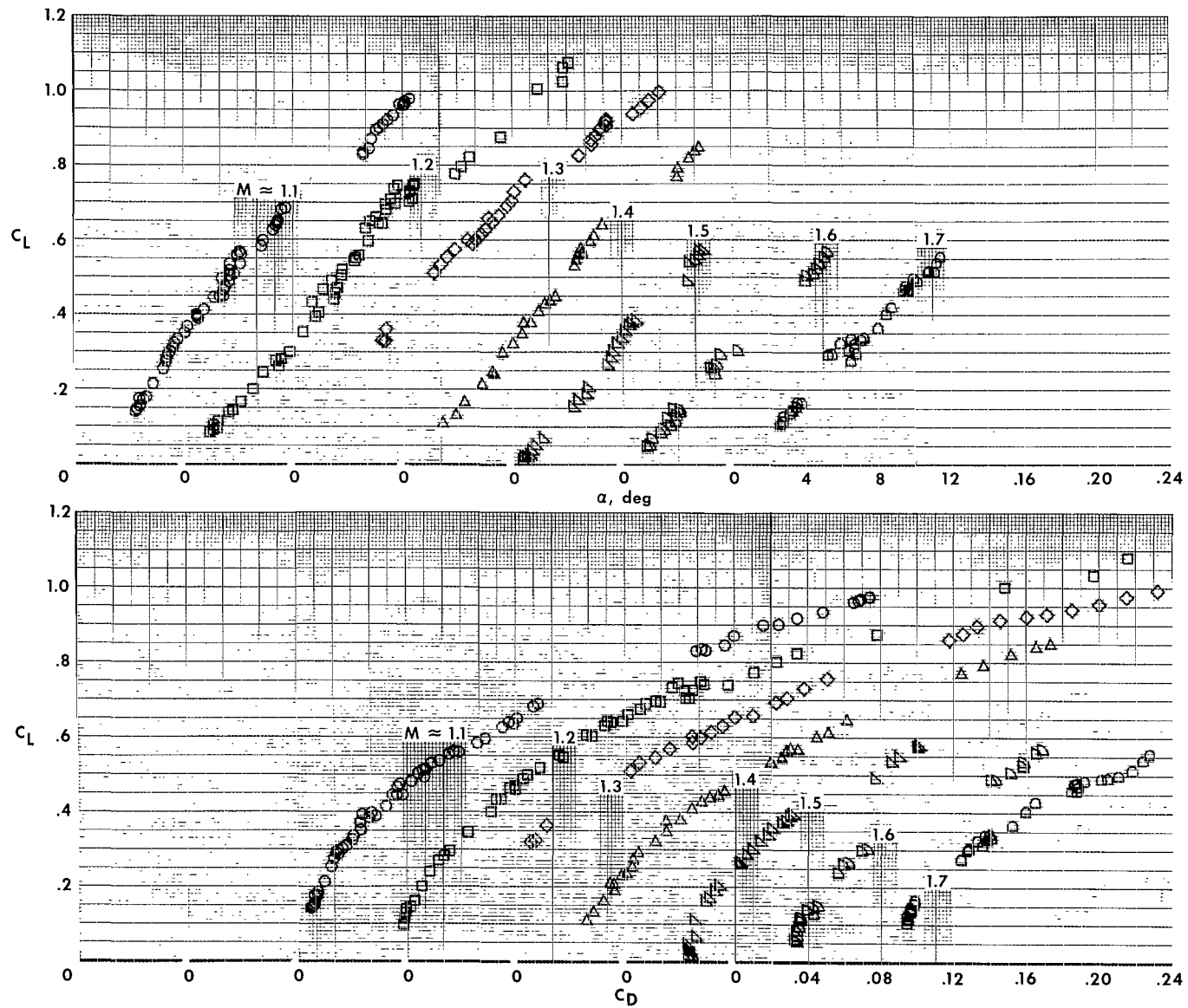


(b) Wing.

Figure 6.- Calculated upwash factors for the angle-of-attack vane location.

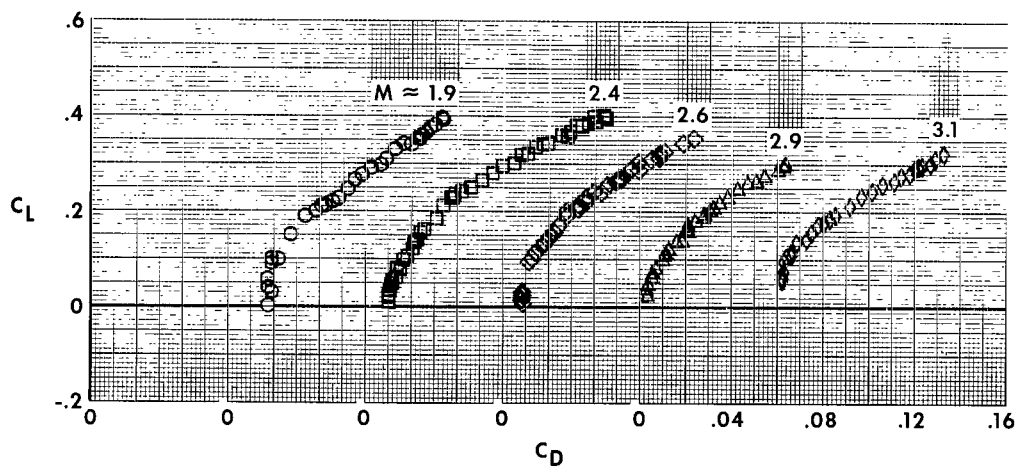
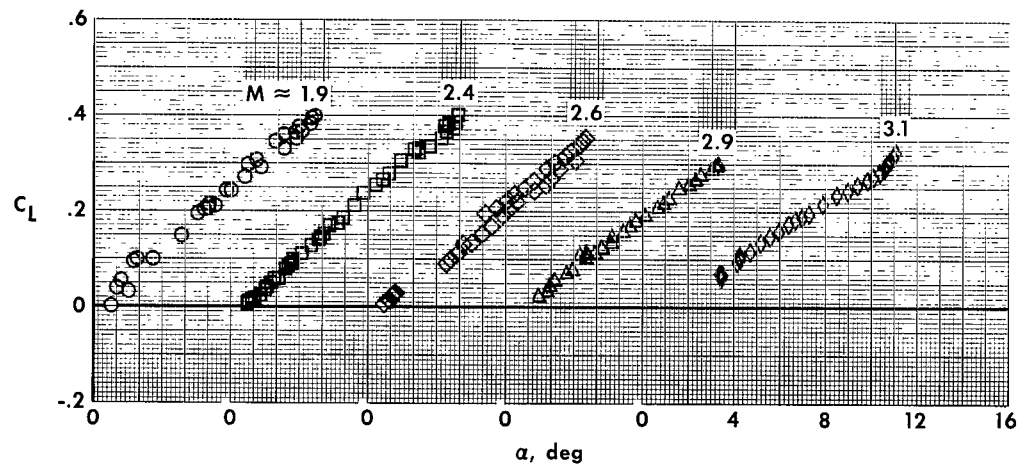


(a) Subsonic speed range, interim configuration.



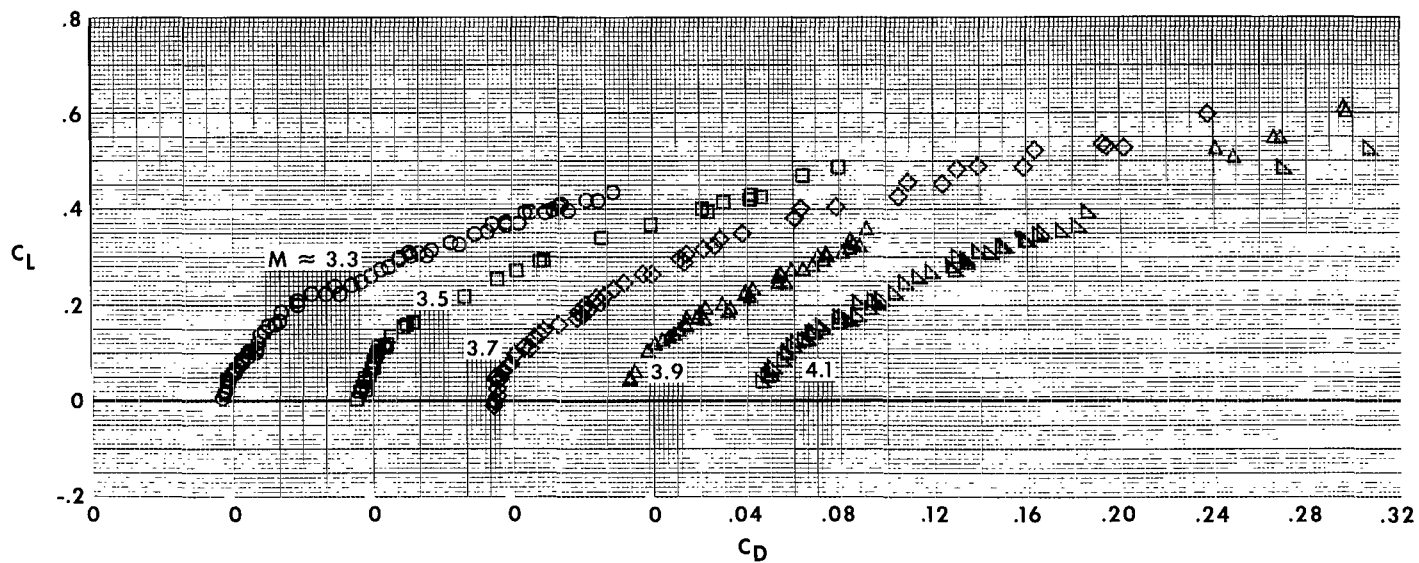
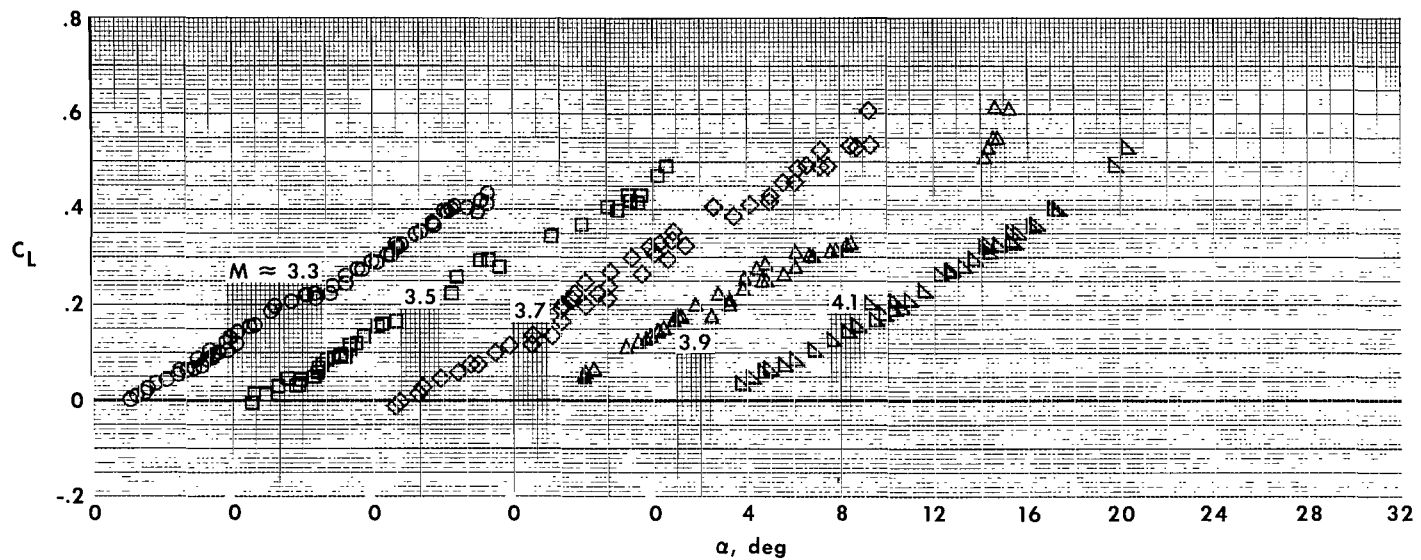
(b) Transonic speed range, interim configuration.

Figure 7.- Continued.



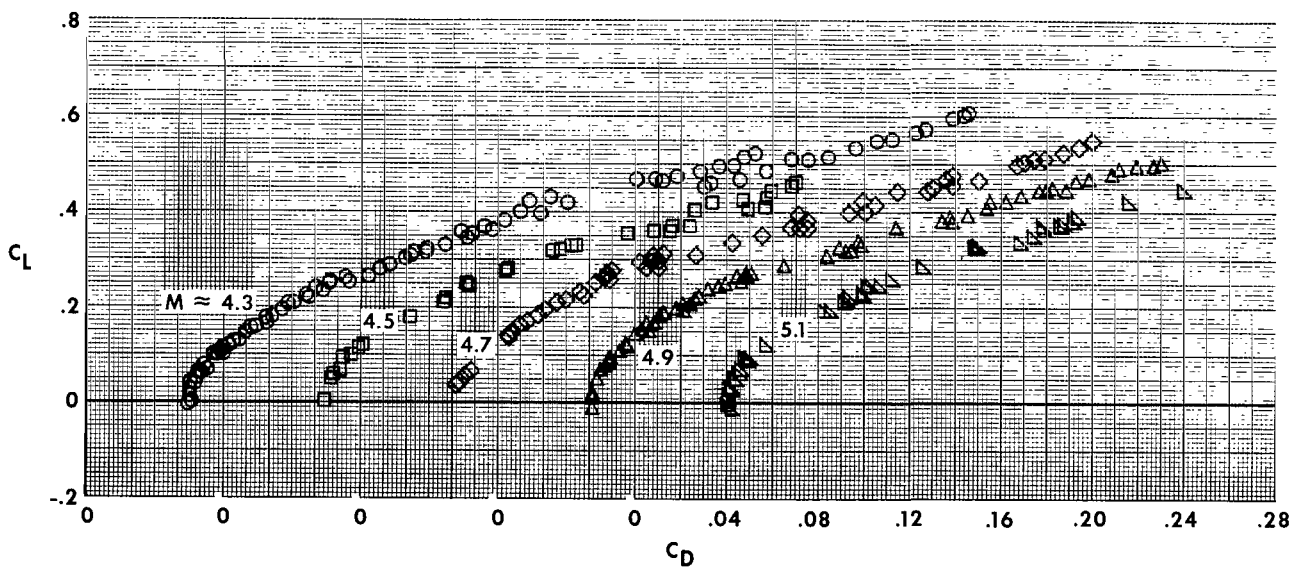
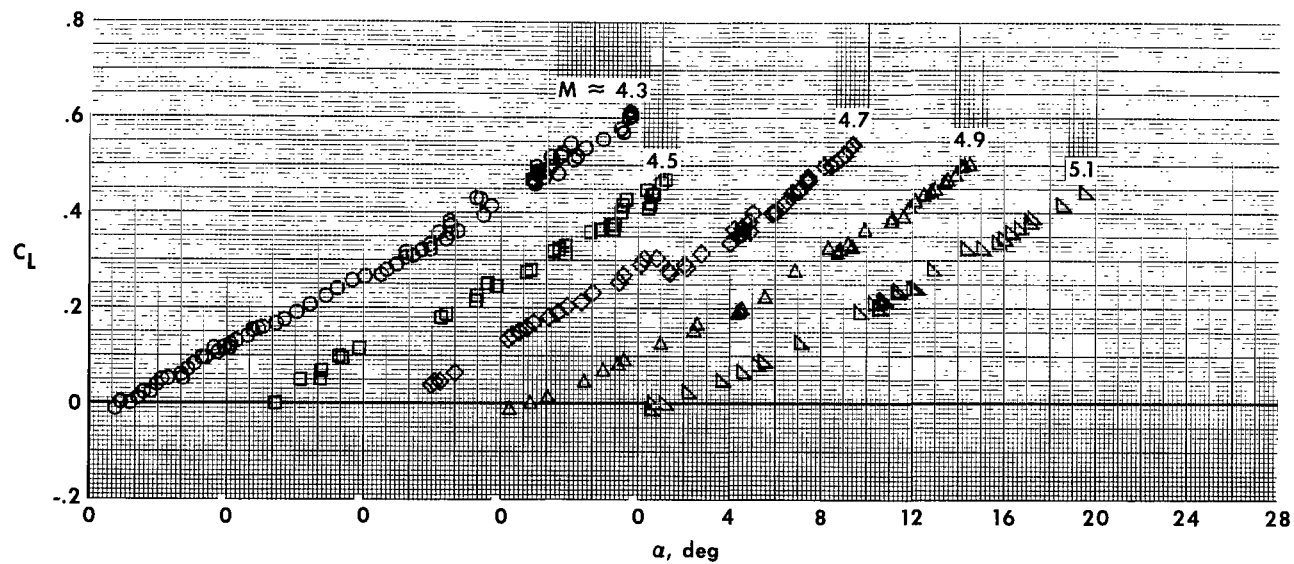
(c) $M \approx 1.9$ to 3.1, interim configuration.

Figure 7.— Continued.



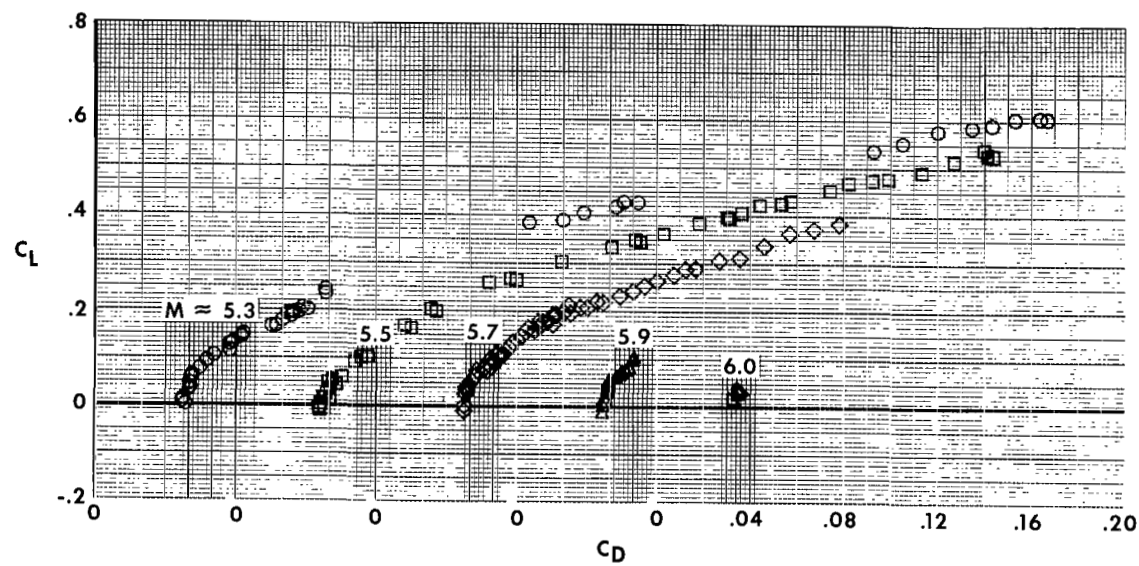
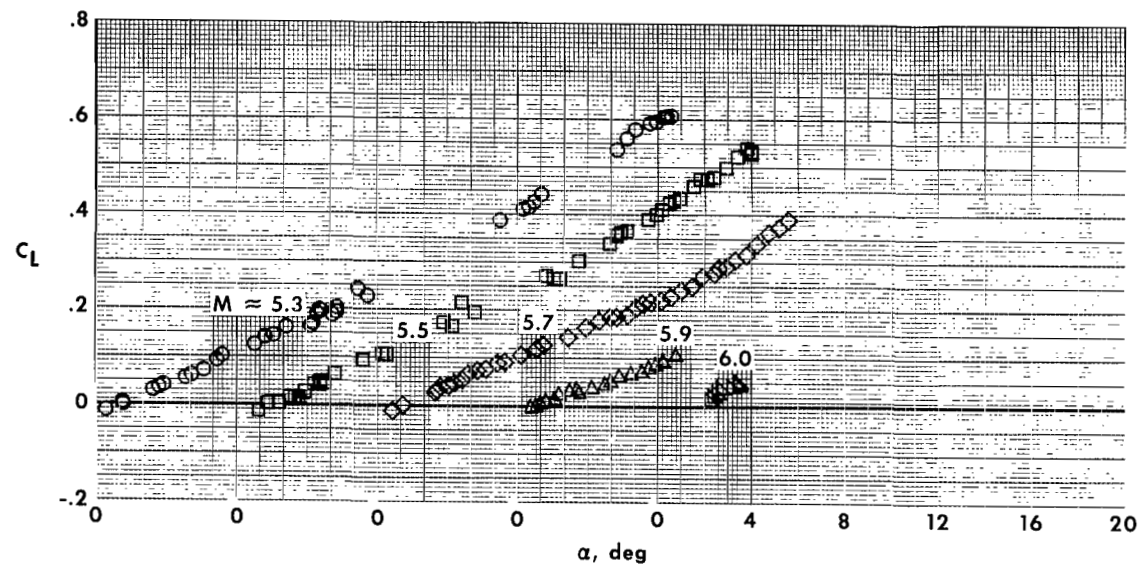
(d) $M \approx 3.3$ to 4.1, basic configuration.

Figure 7.- Continued.



(e) $M \approx 4.3$ to 5.1, basic configuration.

Figure 7.— Continued.



(f) $M \approx 5.3$ to 6.0, basic configuration.

Figure 7.— Concluded.

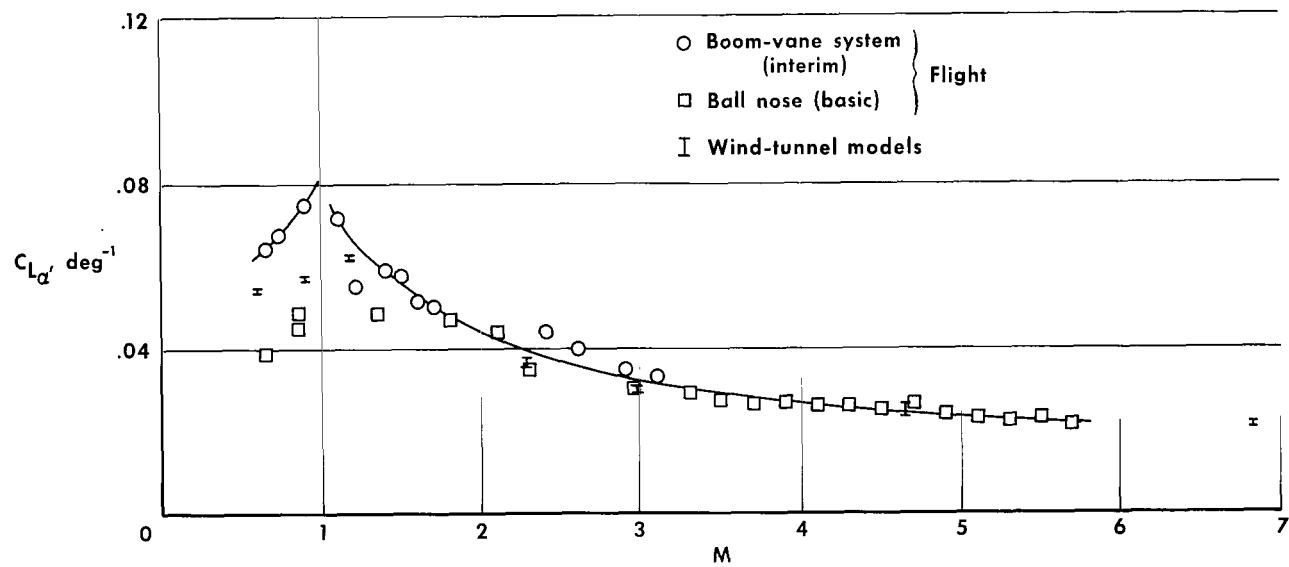


Figure 8.— Lift-curve-slope variation with Mach number. Trimmed.

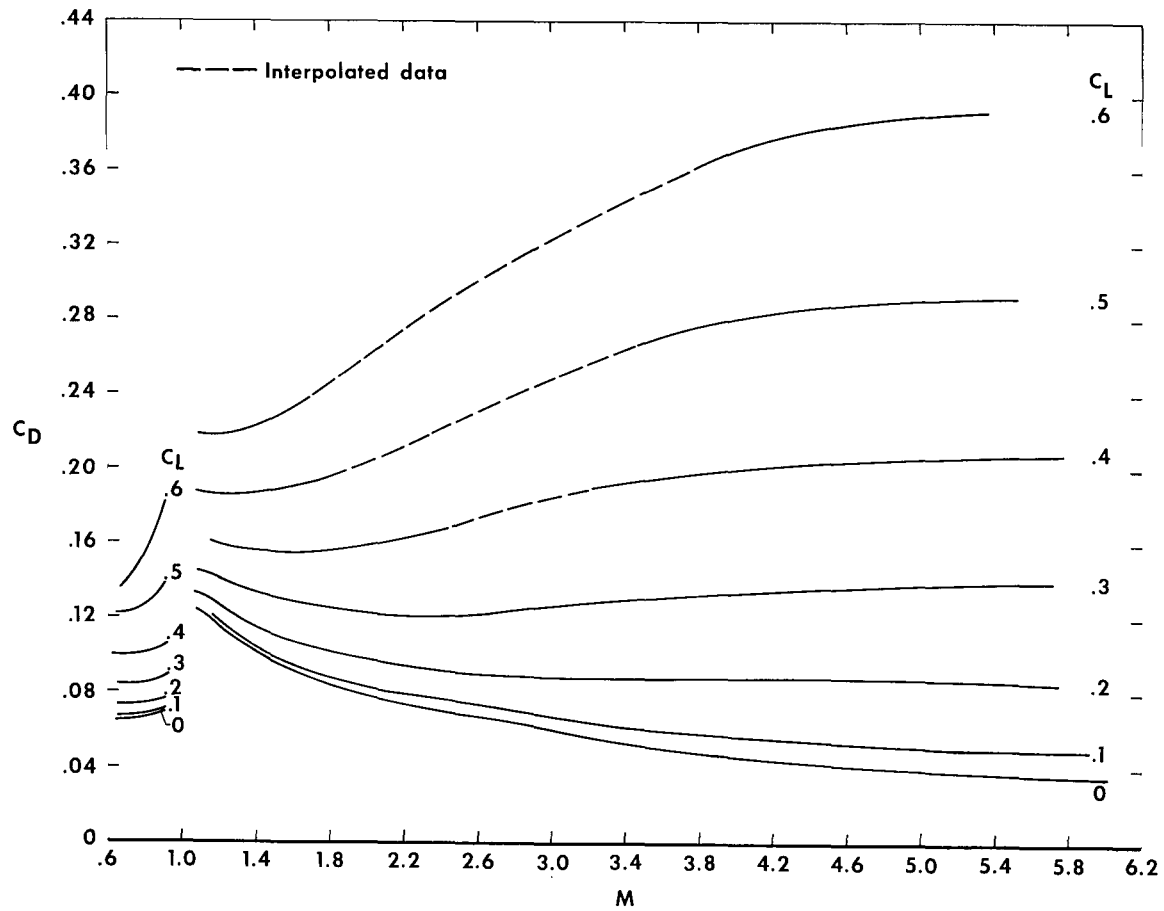


Figure 9.— Variation of drag coefficient with Mach number for constant values of lift coefficient. Trimmed flight.

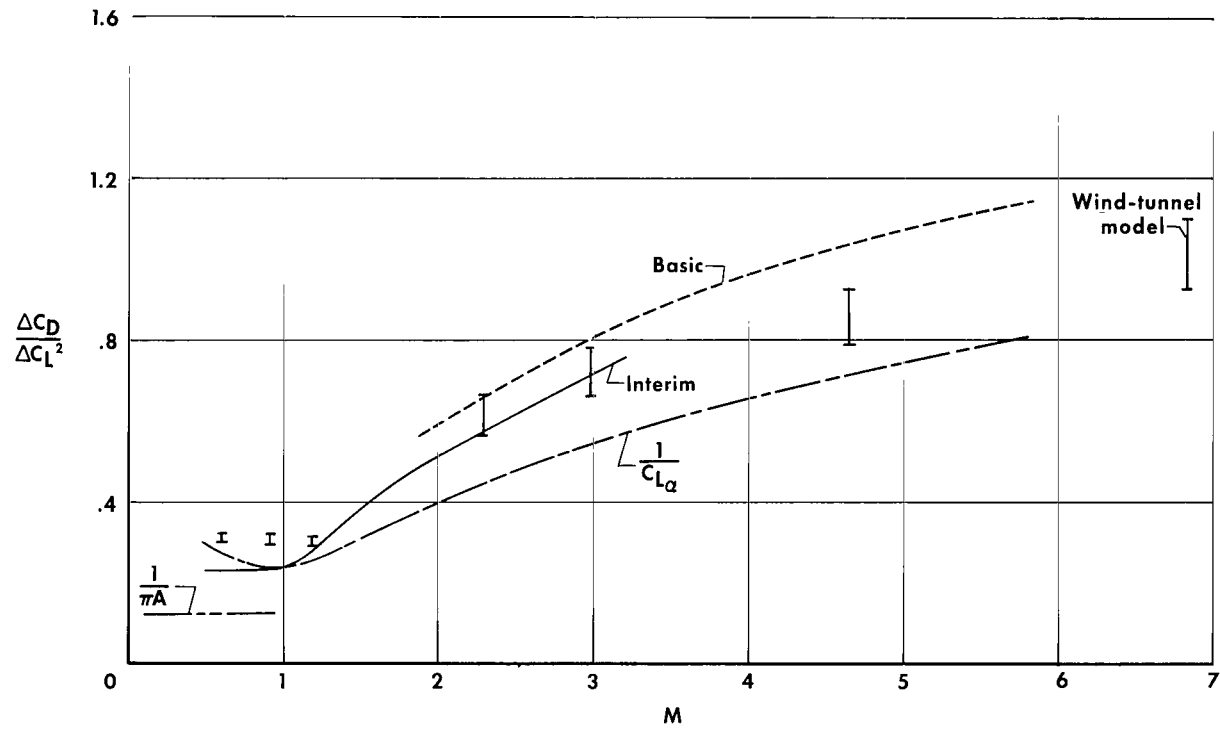


Figure 10.— Variation of trimmed drag-due-to-lift factor with Mach number.

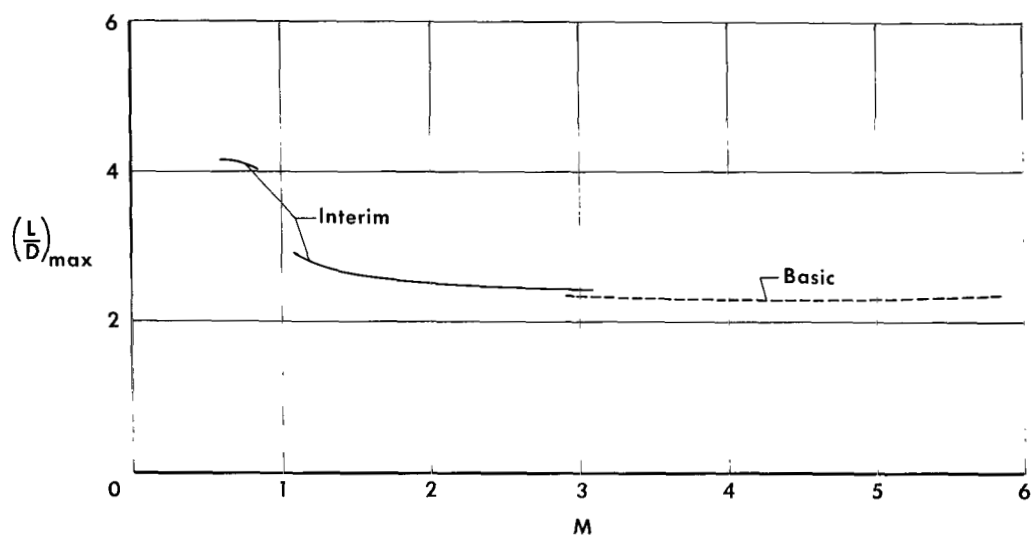


Figure 11.- Variation of $(L/D)_{\max}$ with Mach number. Trimmed flight.

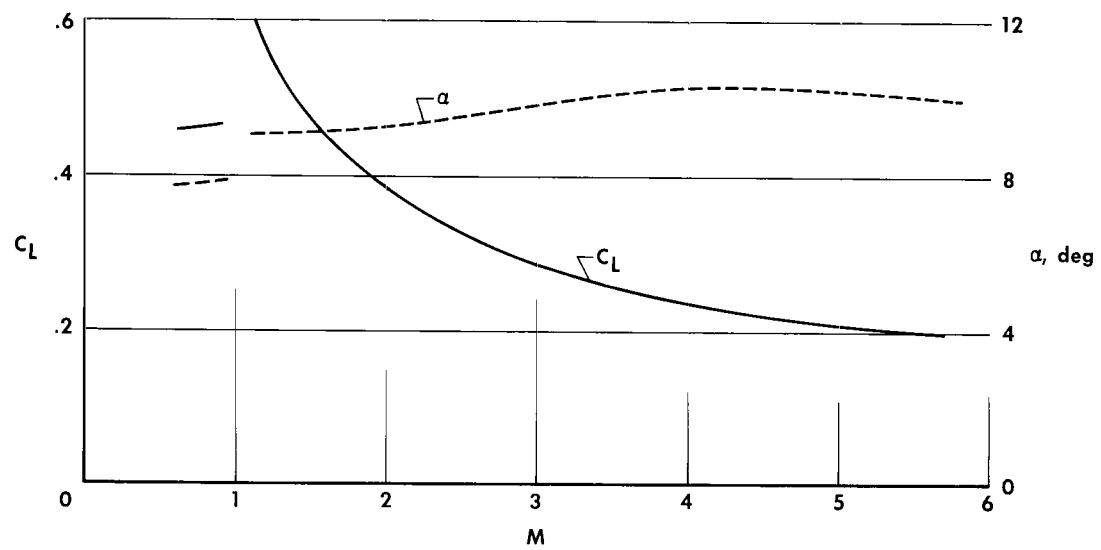
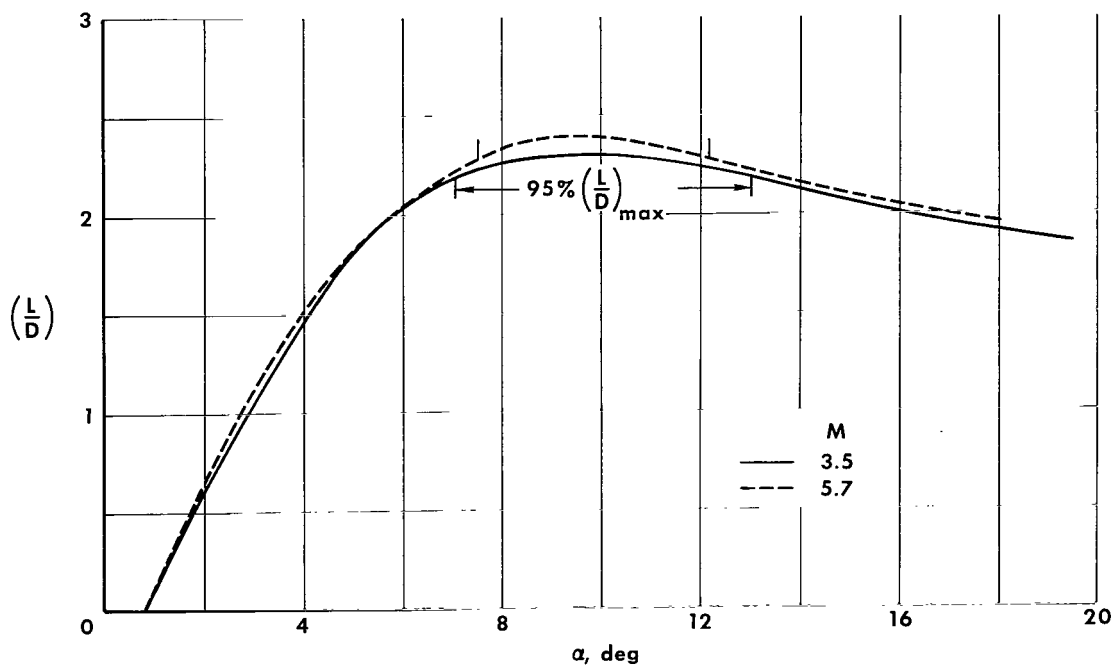
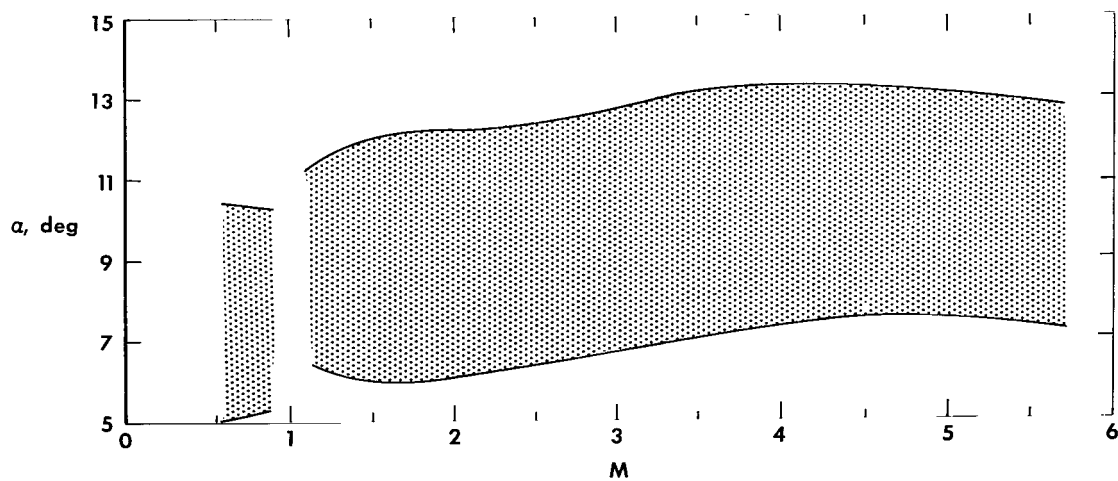


Figure 12.— Lift coefficient and angle of attack required to achieve maximum lift-drag ratio in trimmed flight.

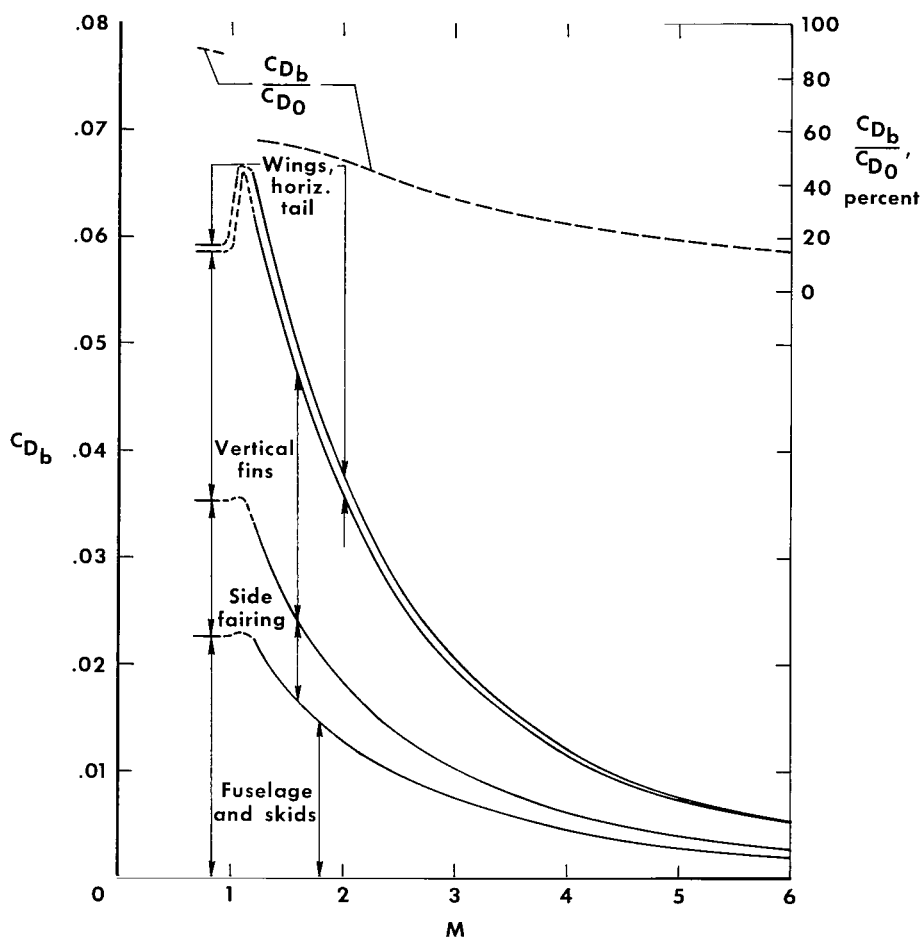


(a) Example of the variation of lift-drag ratio with angle of attack.
Ticks indicate α range for 95-percent $(L/D)_{\max}$.



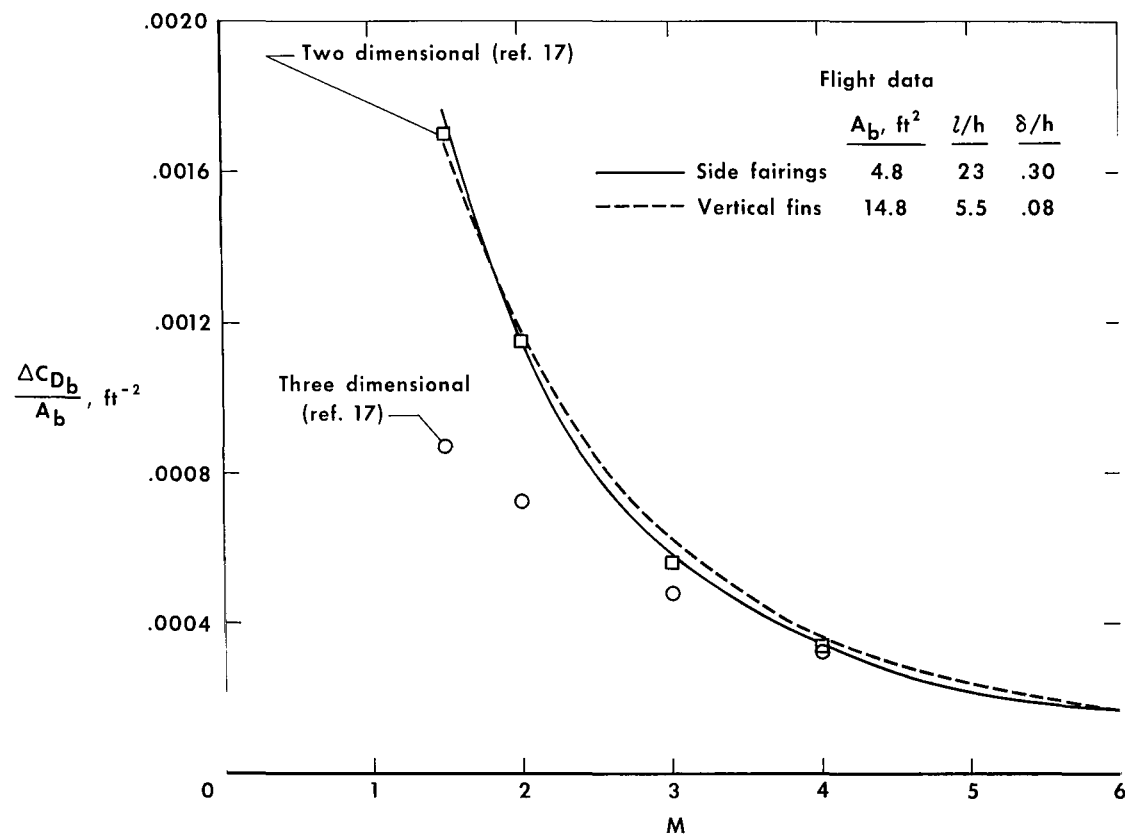
(b) Range of angle of attack over which 95 percent of $(L/D)_{\max}$ is obtainable.

Figure 13.— Relationship of maximum lift-drag ratio to angle of attack.



(a) Base-drag coefficient.

Figure 14.— Variation of flight base-drag characteristics with Mach number.



(b) Increment of base-drag coefficient per unit area for different forebodies.

Figure 14.- Concluded.

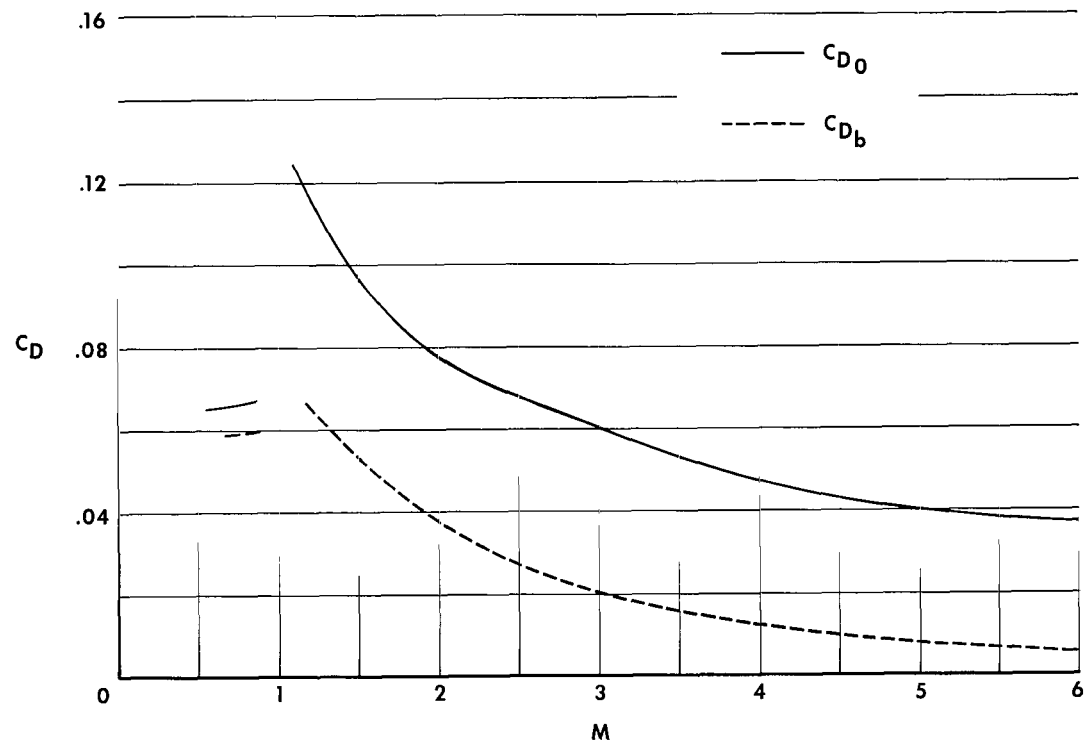


Figure 15.— Comparison of zero-lift drag and base drag. Power-off flight.

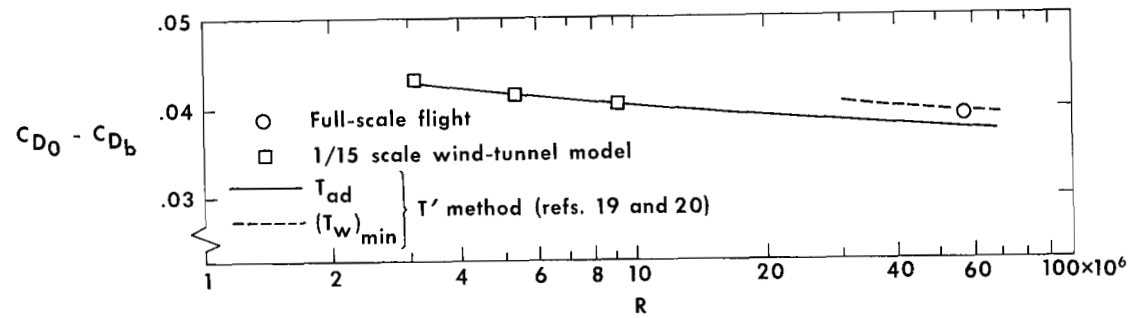
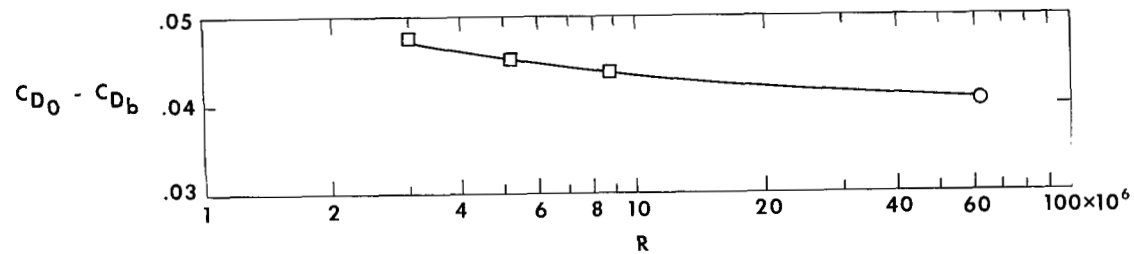
(a) $M = 3.0$.(b) $M = 2.5$.

Figure 16.— Effect of Reynolds number on zero-lift drag coefficient minus base-drag coefficient. Turbulent flow; power off.

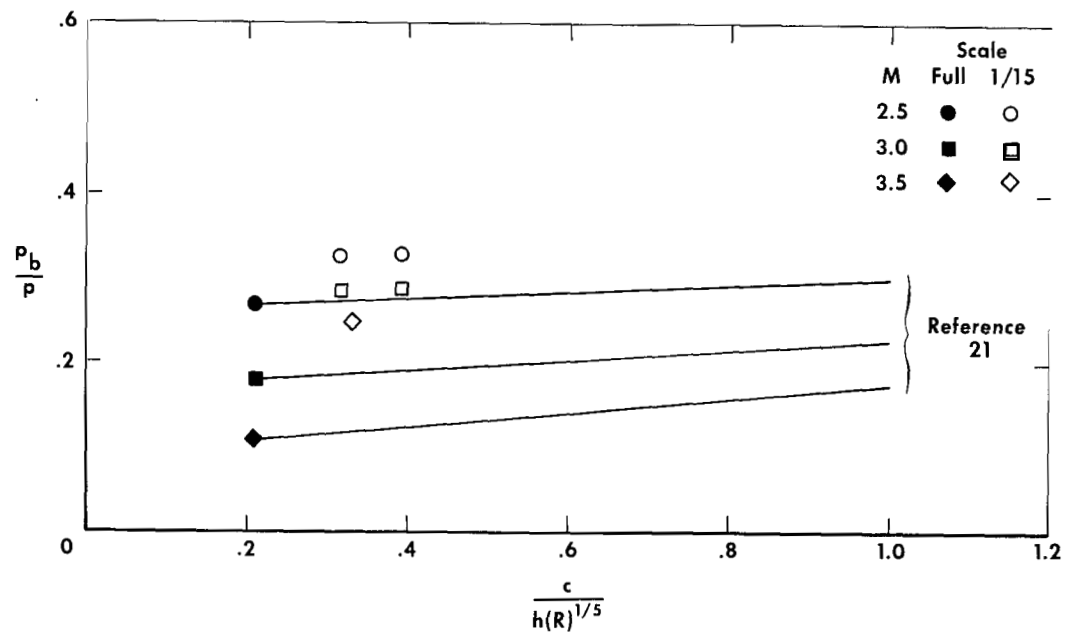


Figure 17.— Base-pressure ratio for the upper vertical fin as determined in full-scale flight and on a wind-tunnel model for turbulent flow.

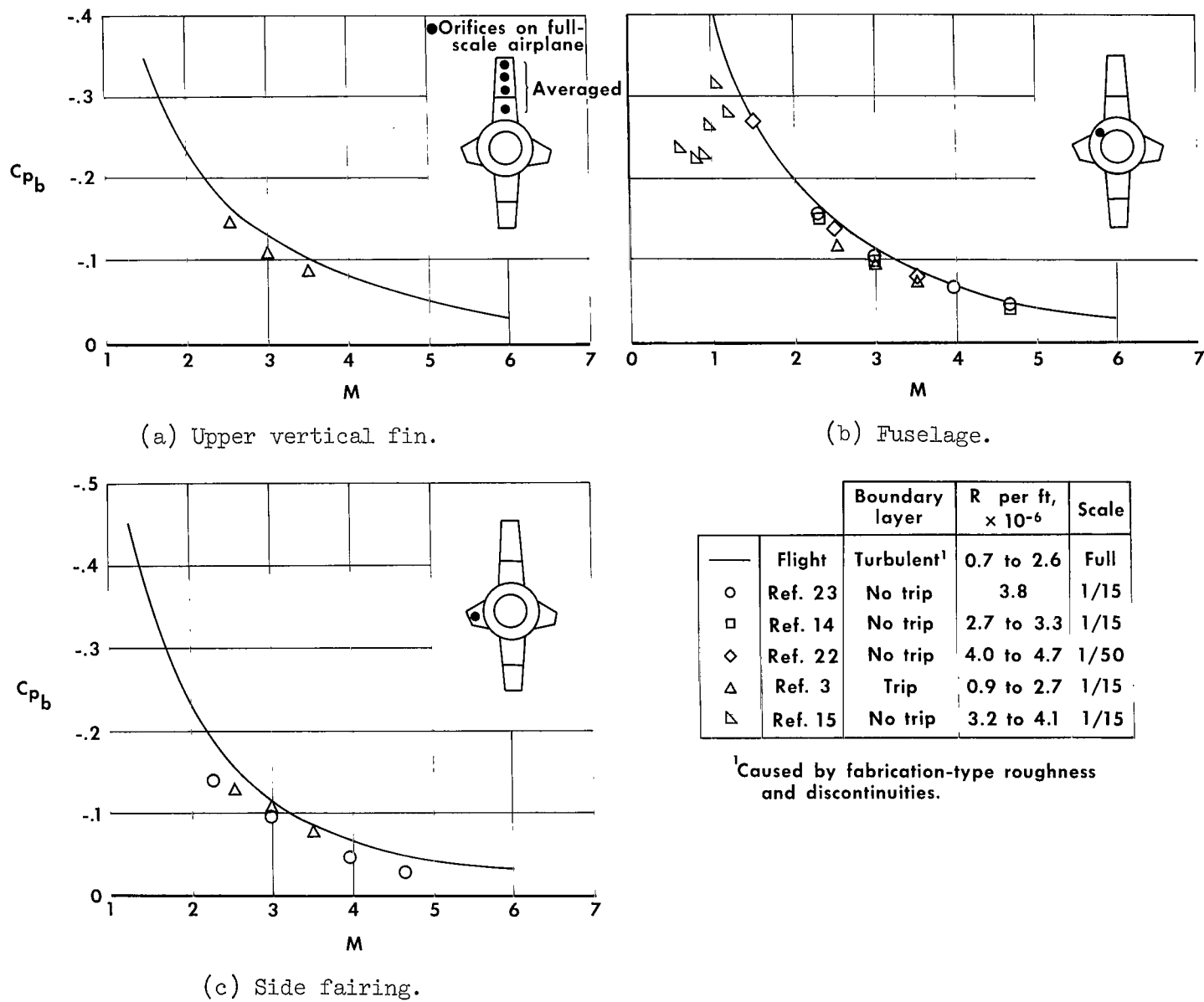
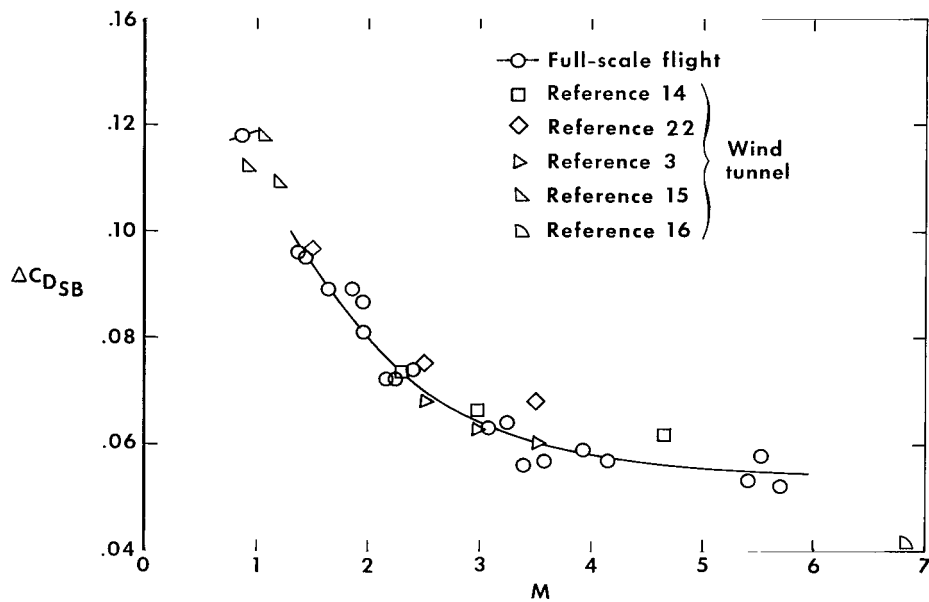
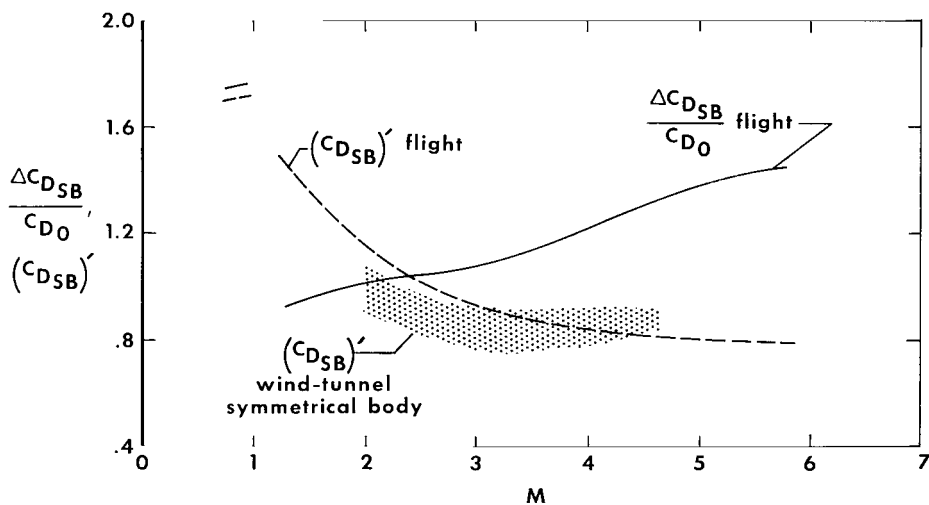


Figure 18.— Comparison of base-pressure coefficients obtained from full-scale flight and X-15 wind-tunnel models. Power off.



(a) Full-scale and model comparison.



(b) Speed-brake drag and zero-lift drag comparison.

Figure 19.— Variation of speed-brake drag with Mach number.

"The aeronautical and space activities of the United States shall be conducted so as to contribute . . . to the expansion of human knowledge of phenomena in the atmosphere and space. The Administration shall provide for the widest practicable and appropriate dissemination of information concerning its activities and the results thereof."

—NATIONAL AERONAUTICS AND SPACE ACT OF 1958

NASA SCIENTIFIC AND TECHNICAL PUBLICATIONS

TECHNICAL REPORTS: Scientific and technical information considered important, complete, and a lasting contribution to existing knowledge.

TECHNICAL NOTES: Information less broad in scope but nevertheless of importance as a contribution to existing knowledge.

TECHNICAL MEMORANDUMS: Information receiving limited distribution because of preliminary data, security classification, or other reasons.

CONTRACTOR REPORTS: Technical information generated in connection with a NASA contract or grant and released under NASA auspices.

TECHNICAL TRANSLATIONS: Information published in a foreign language considered to merit NASA distribution in English.

TECHNICAL REPRINTS: Information derived from NASA activities and initially published in the form of journal articles.

SPECIAL PUBLICATIONS: Information derived from or of value to NASA activities but not necessarily reporting the results of individual NASA-programmed scientific efforts. Publications include conference proceedings, monographs, data compilations, handbooks, sourcebooks, and special bibliographies.

Details on the availability of these publications may be obtained from:

SCIENTIFIC AND TECHNICAL INFORMATION DIVISION
NATIONAL AERONAUTICS AND SPACE ADMINISTRATION
Washington, D.C. 20546